

# Audio-visual cross-modality knowledge transfer for machine learning-based in-situ monitoring in laser additive manufacturing

Jiarui Xie <sup>a</sup>, Mutahar Safdar <sup>a</sup>, Lequn Chen <sup>b,c,\*</sup>, Seung Ki Moon <sup>b</sup>, Yaoyao Fiona Zhao <sup>a,\*</sup>

<sup>a</sup> Department of Mechanical Engineering, McGill University, Montreal, Quebec, Canada, H3A 0G4

<sup>b</sup> School of Mechanical and Aerospace Engineering, Nanyang Technological University, Singapore, 639798

<sup>c</sup> Advanced Remanufacturing and Technology Center (ARTC), Agency of Science, Technology and Research (A\*STAR) Singapore, 637143

\* Corresponding authors.

Email addresses: yaoyao.zhao@mcgill.ca (Y. F. Zhao) and chen1470@e.ntu.edu.sg (L. Chen)

## Abstract

Various machine learning (ML)-based in-situ monitoring systems have been developed to detect laser additive manufacturing (LAM) process anomalies and defects. Multimodal fusion can improve in-situ monitoring performance by acquiring and integrating data from multiple modalities, including visual and audio data. However, multimodal fusion employs multiple sensors of different types, which leads to higher hardware, computational, and operational costs. This paper proposes a cross-modality knowledge transfer (CMKT) methodology that transfers knowledge from a source to a target modality for LAM in-situ monitoring. CMKT enhances the usefulness of the features extracted from the target modality during the training phase and removes the sensors of the source modality during the prediction phase. This paper proposes three CMKT methods: semantic alignment, fully supervised mapping, and semi-supervised mapping. Semantic alignment establishes a shared encoded space between modalities to facilitate knowledge transfer. It utilizes a semantic alignment loss to align the distributions of the same classes (e.g., visual defective and audio defective classes) and a separation loss to separate the distributions of different classes (e.g., visual defective and audio defect-free classes). The two mapping methods transfer knowledge by deriving the features of one modality from the other modality using fully supervised and semi-supervised learning. The proposed CMKT methods were implemented and compared with multimodal audio-visual fusion in an LAM in-situ anomaly detection case study. The semantic alignment method achieves a 98.4% accuracy while removing the audio modality during the prediction phase, which is comparable to the accuracy of multimodal fusion (98.2%).

**Keywords:** Multimodal; machine learning; knowledge transfer; additive manufacturing; process monitoring; data fusion

## Nomenclature

Abbreviation	Full phrase
AM	Additive manufacturing
LAM	Laser additive manufacturing
ML	Machine learning
KNN	K-nearest neighbors
LPBF	Laser powder bed fusion
IoT	Internet of Things
CNN	Convolutional neural network

LDED	Laser direct energy deposition
LoF	Lack of fusion
WAAM	Wire arc additive manufacturing
CMKT	Cross-modality knowledge transfer
CCD	Charge-coupled device
ROS	Robot operating system
TP	True positive
TN	True negative
FP	False positive
FN	False negative
TPR	True positive rate
FPR	False positive rate
TNR	True negative rate
AUC	Area under the curve
ROC	Receiver operating characteristics
AUC-ROC	Area under the Receiver operating characteristics curve
t-SNE	t-distributed stochastic neighbor embedding

## 1. Introduction

Additive Manufacturing (AM) or 3D printing-based techniques fabricate parts in a layer-upon-layer manner as opposed to conventional manufacturing techniques based on material removal [1]. AM offers several benefits such as tool elimination, material savings, design freedom, part consolidation, prototyping ease, and mass customization. These AM features unlock constraints on product design and production efficiency and have a significant economic potential [2]. AM technologies also enable specialized applications such as the printing of multifunctional or multi-material designs. Despite their merits, AM techniques also suffer from a multitude of process defects and process anomalies limiting their adoption for large-scale industrial production [3,4]. The potential of AM to offer unique solutions to new and existing challenges in design and manufacturing has inspired a multi-faceted research landscape spanning materials, hardware, and software development [5,6].

AM process development has seen numerous research efforts focused on advanced monitoring techniques [3]. These efforts are fueled by the process complexity (e.g., hardware, software, and material aspects), range of physical scale (e.g., microscopic to macroscopic), domain diversity (e.g., spatial and/or temporal), and information magnitude (e.g., frequency, volume, and variety) [7,8]. The motivation to monitor rests in the potential to capture information associated with defective or anomalous features from process phenomena (interactions, melting, re-melting, and cooling) or physical objects (melt pools, layers, and under-build parts) for downstream analytics applications [9]. Chen et al. [10] recently reviewed in-situ monitoring techniques for laser-based AM and grouped them into optical, acoustic, laser-line scanning, and multi-sensor-based categories. Each category offers unique merits suiting diverse downstream applications such as process state prediction, defect detection or classification, and property or performance estimation [9]. The rise of multi-sensor fusion techniques hints at the potential of overcoming the limitations faced by individual monitoring approaches and opens the possibility of knowledge transfer across information modalities [11].

The in-situ data collected from process monitoring systems can be used to train machine learning (ML) models for various AM tasks, including process anomaly detection, defect detection, and quality prediction [10]. For example, metal AM process anomaly detection models can be trained using vision-based melt pool monitoring data to identify the locations of potential defects [12]. Image segmentation models trained on labeled layer-wise AM images can classify defects at the pixel level [13]. Combined with process parameters and part geometry information, in-process data can also be used to infer the part quality such as geometric conformity and mechanical properties [14]. According to the defect detection and quality prediction results, process parameters can be adjusted to enhance the part quality. Although ML-based AM process monitoring systems offer abundant potential for improving AM process reliability, they have not been extensively deployed in real-life production environments. The costs of monitoring instruments and data acquisition might not be sufficiently compensated by the enhanced part quality [10]. Besides, the quality control standards of industrial production demand high performance from AM process modeling results.

Multisensor monitoring and data fusion have been recently implemented to enrich data informativeness for modeling performance improvement [15,16]. This method is founded on the assumption that a single sensor only captures part of the physical phenomena of the AM process; thus, the collected dataset is likely to have missing information about the modeling task. Multisensor fusion utilizes data from multiple sensors to complement each other and fill the information gap. Multimodal fusion is a special type of multisensor fusion that integrates datasets of different modalities, including vision-based, acoustic-based, and thermal-based data [17]. Multisensor and multimodal fusion have been proven effective in laser powder bed fusion (LPBF) defect detection [17,18] and quality prediction [16]. However, the improved predictive performance is accompanied by higher costs and data volume, making AM process monitoring less affordable. A multisensor system considerably increases the deployment cost because of the expenses associated with the purchase, operation, and maintenance of multiple sensors. Moreover, the enlarged data volume of multisensor fusion increases data handling and model prediction runtime. This requires a powerful computation capacity to ensure real-time defect detection and process control, further increasing the cost. In an Internet of Things (IoT) setting where data are wirelessly transmitted to the cloud, a large data volume leads to high power consumption and long transmission time.

The recent research advancements in LAM in-situ monitoring focus on model developments integrating comprehensive information and complex ML architectures, while often overlooking and complicating model deployment. As discussed above, multimodal fusion improves the predictability of LAM processes, but the high operational and computational costs impede its deployment in real production. To improve deployability, this paper proposes a cross-modality knowledge transfer (CMKT) methodology to reduce the data volume and sensor costs while retaining comparable performance. In multimodal fusion, data from multiple modalities are collected in both the training and prediction phases (Figure 1a). In contrast, CMKT only collects data from multiple modalities in the training phase, where knowledge is transferred from the source modality to the target modality (Figure 1b). The proposed methodology removes the source modality and utilizes the target modality as the input during the prediction phase, thus enhancing operational and computational efficiencies. The key contributions of this paper are summarized below:

- This paper proposes a CMKT methodology that integrates in-situ laser direct energy deposition (LDED) visual and audio data and transfers knowledge between the two modalities.
- A semantic alignment CMKT method is proposed to semantically align the visual and audio modalities of in-situ LDED data in a shared encoded space.
- Two cross-modality mapping methods are proposed to conduct CMKT by deriving the features of the source modality from the target modality for in-situ LDED data.
- The proposed CMKT methods are implemented to train LDED process anomaly detection models leading to higher performance.
- This paper compares the CMKT methods and multimodal fusion methods based on predictive performance, computational complexity, and operational efficiency.

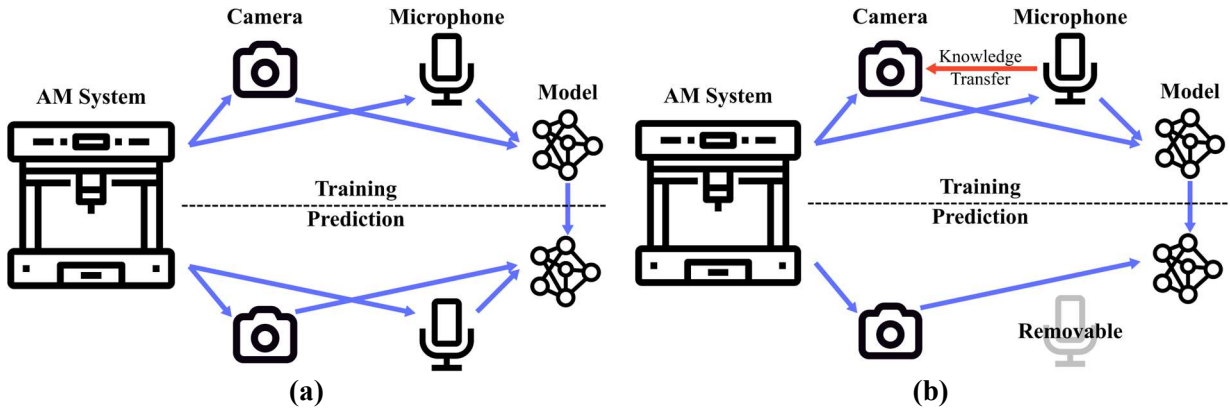


Figure 1: System setups of (a) multimodal fusion and (b) cross-modality knowledge transfer.

The remainder of this paper is organized as follows. Section 2 reviews AM process monitoring and knowledge transfer, followed by the highlights of the research gaps. Section 3 elaborates on the experiment, dataset, and proposed CMKT methods. Section 4 illustrates the training and evaluation of the CMKT and multimodal fusion models. Section 5 discusses the modeling results regarding predictive performance, computational complexity, and operational efficiency. Section 6 highlights the remarks of this research.

## 2. Related research

This section examines the current state of ML-assisted in-situ process monitoring in LAM, emphasizing acoustic and vision-based techniques. Each sensing modality offers unique insights into the LAM process. Here, we explore their inherent limitations and introduce knowledge transfer as a potential solution to these challenges. Additionally, we extend the discussion to CMKT, illustrating its applications in other advanced fields and proposing its novel integration into LAM to improve in-situ process monitoring and defect detection.

### 2.1. ML-assisted process monitoring in LAM

Early defect detection and correction are crucial for ensuring part quality and enhancing the reliability of LAM processes. ML-assisted in-situ process monitoring plays a pivotal role in achieving this by capturing dynamic laser-material interactions within the melt pool [19–22].

Among the various monitoring technologies, vision-based monitoring is particularly notable for its ability to directly observe and analyze melt pool dynamics. The data captured through

coaxial cameras can reflect essential metallurgical phenomena such as melting, cooling, and heat transfer [23–25]. Researchers have focused on extracting physics-informed features from these images as quality indicators for predicting process anomalies and defects [26–29]. Features like melt pool morphologies and temperature, influenced by input energy density, have been correlated with process stability [30]. For instance, Khanzadeh et al. [31] used a k-nearest neighbors (KNN) model to analyze melt pool geometries and predict porosity in real-time from X-ray tomography-labeled melt pool pictures with 98.44% accuracy. Similarly, Ren et al. [32] implemented a convolutional neural network (CNN) model based on high-speed synchrotron X-ray and thermal imaging to detect keyhole pores in LPBF of Ti-6Al-4V, achieving submillisecond temporal resolution and near-perfect prediction rates. Moreover, Asadi et al. [33] proposed a YOLOv8l model for in-situ melt pool segmentation of the LDED process, achieving high accuracy in predicting bead geometry. Other examples include using off-axis thermal imaging in LPBF, which demonstrates success in localized porosity prediction [34,35].

Despite these advancements, the implementation of vision-based monitoring remains expensive and time-consuming. Moreover, integrating vision sensors into existing setups often requires customized hardware designs, which increases costs and deployment complexity. In contrast, acoustic-based monitoring offers a compelling alternative. This technique utilizes acoustic signals generated by laser-material interactions, which contain rich information about processes such as melting, solidification, and defect formation [36–39]. Unlike visual sensors, acoustic monitoring does not require extensive modifications to AM equipment, facilitating easier integration and operation. Recent studies have demonstrated the potential of acoustic signals in predicting pore concentrations and classifying lack of fusion (LoF), keyhole pores, and cracks through ML [40–44].

To further enhance the robustness of process monitoring, the integration of multisensor approaches is advocated [45–50]. By combining data from different sensing modalities, multisensor models address the limitations inherent to single-sensor setups. This method leverages the strengths of each sensor type, enabling a comprehensive analysis of the complex, multi-dimensional phenomena occurring within LAM processes. For example, Li et al. [51] developed a feature-level fusion technique, in which photodiode signal and audio signal were fused using a CNN-based model to estimate layer-wise LPBF quality. Chen et al. [50] proposed a hybrid CNN model which incorporates visual and audio feature extraction streams to achieve localized quality prediction in robotic LDED. Similar research on multisensor fusion in LAM monitoring has also been conducted in [52–54]. These studies showed that combining sensing modalities enhances defect detection accuracy and process dynamics understanding.

Despite the promising results of acoustic-based monitoring, their robustness and accuracy still lag behind those of vision-based approaches, particularly in the LDED process where noise can degrade acoustic signal quality [43]. Although multisensor approach can enhance overall prediction accuracy, such methods often require expensive sensor setups and are generally not favored by industry end-users. Recently, Liu et al. [55] proposed a method that utilizes combined acoustic and photodiode signals to infer melt pool morphological features and predict spatially-dependent LoF defects in LPBF. Similarly, visual characteristics of the melt pool in LDED can be inferred from more cost-effective audio modality [56]. This indicates the possibility of transferring knowledge from one sensing modality to another, which could lead to even better outcomes.

## **2.2. Knowledge transfer for in-situ process monitoring in LAM**

Knowledge transfer has emerged as a powerful strategy in ML, particularly useful in domains where data are scarce or expensive to collect, such as in LAM [57]. This subsection discusses various types of knowledge transfer applied for process monitoring in LAM, categorizing them based on their application scope: knowledge transfer from public datasets to domain-specific small datasets, from one material to another, and from one process to another (e.g., from LPBF to LDED).

### **2.2.1. Public to domain-specific dataset transfer**

In LAM, the scarcity of large, annotated datasets often impedes the application of deep learning techniques. A pragmatic solution is to leverage knowledge transfer from large, public datasets to smaller, domain-specific ones. For example, Fischer et al. [58] utilized this approach by employing the Xception architecture, initially pretrained on ImageNet, to monitor powder bed quality in LPBF. The proposed method achieved a classification accuracy of 99.15% by distinguishing various inhomogeneities in the powder bed using high-resolution images obtained under different lighting conditions. This approach not only boosts the performance with limited data but also significantly reduces the need for extensive data collection. Similarly, Li et al. [59] demonstrated the effectiveness of knowledge transfer in enhancing in-situ quality inspection in the LPBF by using model pretrained on ImageNet and re-trained on layer-wise visual images. Zhu et al. [60] addressed the challenge of small dataset sizes in detecting surface defects in LDED, where knowledge transfer was used to pretrain a YOLOv7 model using an open-source defect dataset (NEU-DEF) and then finetuned it with a small dataset of LDED surface images. The results demonstrated an improved accuracy and an accelerated convergence of the model.

### **2.2.2. Cross-material and cross-process transfer**

The versatility of knowledge transfer extends beyond dataset enhancement to enable knowledge transfer across different materials and manufacturing processes. Pandiyan et al. [61] explored this by training deep learning models on acoustic emissions from LPBF of stainless steel and successfully transferring the learned features to monitor LPBF of bronze. This cross-material transferability showcases the potential to generalize models across different materials, significantly reducing the model training time and the need for extensive new data collection for each material type. Similarly, Shin et al. [62] employed multisource knowledge transfer to detect balling defects in wire arc additive manufacturing (WAAM), by extracting features from multiple materials and finetuning the model for specific anomaly detection. Li et al. [63] conducted knowledge transfer from 316L stainless steel to TC4 titanium alloy for LPBF quality prediction based on a multisensor dataset, including layer-wise images, photodiode signals, and acoustic emission signals.

Knowledge transfer also facilitates the bridging of knowledge between difference in process maps, adapting models to handle variations in process parameters and environmental conditions effectively [64]. For example, Pandiyan et al. [65] employed unsupervised domain adaptation techniques to manage shifts in data distribution caused by different process parameter spaces in LPBF. Furthermore, knowledge transfer from one process to another is possible. Safdar et al. [66] proposed a structured framework for transferring data-driven knowledge between metal AM processes, such as from LPBF to LDED. The authors presented a three-step framework that supports the systematic transfer of knowledge at various levels, including data representation and model parameters, which enables efficient cross-process adaptations.

Overall, knowledge transfer offers substantial benefits in addressing the challenges of data scarcity and the high cost of data collection in LAM. By pretraining models on public domain datasets, this approach enables high defect detection accuracy with smaller, domain-specific datasets. In addition, it facilitates the transfer of knowledge from one material to another and between similar processes, such as from LPBF to LDED, both of which are fusion-based metal AM techniques. Despite these advancements, the potential for knowledge transfer from one sensing modality to another remains largely unexplored. This gap is significant because information from a superior modality, such as thermal images or coaxial melt pool images, could be transferred to more cost-effective modalities such as acoustic signals.

### 2.3. Cross-modality knowledge transfer

Cross-modality knowledge transfer leverages different data modalities to enrich learning models, overcoming limitations specific to one type of data through the integration of another. This subsection systematically explores how this concept has been applied across various fields, enhancing model effectiveness and data utilization.

Athanasiadis et al. [67] tackled the challenge of emotion recognition, traditionally limited by the high costs and ambiguities of audio data annotation. By employing conditional semi-supervised generative adversarial networks, they fused facial expressions from images with audio signals to predict emotions more accurately. This cross-modality approach leveraged the rich, annotated visual data to compensate for the sparse audio annotations, demonstrating improved classification performance and the potential of visual data to enhance audio-based models. Similarly, Zhang et al. [68] introduced a combination of CMKT with semi-supervised learning. They used visual features to enhance the diversity and reliability of pseudo-labels in audio data, increasing the robustness and accuracy of speech (audio) model. This approach addressed the scarcity of labeled speech datasets and also mitigated the noise. Planamente et al. [69] addressed first-person action recognition problem, where environmental variability poses significant challenges. They developed an audio-visual loss that aligns the norm magnitudes of features from both modalities, enhancing the model’s ability to generalize across different domains. Zhang et al. [70] explored activity recognition across visual and audio domains affected by changes such as scenery or camera viewpoint. They proposed an audio-adaptive encoder to adjust visual features based on audio features, reducing domain-specific biases and enhancing cross-domain applicability. This strategy highlighted the stabilizing effect of audio data on visual feature representations, especially in varied recording conditions. Cangea et al. [71] proposed a set of deep learning architectures for audio-visual classification that facilitates early integration of cross-modality data flows. This method harnessed the correlations between audio and visual data, enhancing the interpretability and performance of the resulting models. Furthermore, Guo et al. [72] introduced a deep visual-audio network for cross-modality retrieval between speech and remote sensing images, providing a solution to the inefficiencies of traditional text-based retrieval methods. By establishing direct associations between image features and audio features, this approach offered a faster and more intuitive way for retrieving images using natural language inputs.

These studies illustrate the effectiveness of CMKT in enhancing model performance, reducing reliance on large, labeled datasets, and improving generalization across varied conditions. While these applications have not yet been explored within the context of process monitoring in LAM, the CMKT principles could potentially be adapted to this field. Integrating audio and visual data, for instance, could lead to more robust monitoring systems capable of operating under diverse conditions with reduced need for extensive data collections. Such cross-modality transfer could

mitigate the disadvantages of expensive visual modalities, which include large data volumes, extensive annotation requirements, and complex sensor setups, while still achieving reliable results from less costly acoustic monitoring. This untapped potential forms the foundation for investigating cross-modality domain adaptation in this study, aiming to enhance the adaptability and efficiency of monitoring systems in LAM.

### 3. Methodology

This section elaborates on the experiment setting and the proposed CMKT methods. The first subsection lays out the experiments that generated the multimodal dataset to demonstrate the effectiveness of the proposed CMKT methods. The second subsection illustrates the theories of the proposed CMKT methods, including semantic alignment, fully supervised mapping, and semi-supervised mapping.

#### 3.1. Experiments and Dataset Descriptions

Figure 2 illustrates an LDED system along with audio-visual sensor setups, presented both schematically and in an actual photograph. The LDED system features a coaxial powder-feeding nozzle and a 1070 nm laser beam, which melts the metal powder materials for layer-by-layer deposition [73]. As the nozzle moves in the feed direction, the deposited material rapidly solidifies in the molten pool area. Two sensors are employed to monitor the dynamics of the melt pool: (1) a coaxial charge-coupled device (CCD) camera, operating at an acquisition frequency of 30 Hz, and (2) a microphone positioned approximately 10 cm from the process zone, with a sampling rate of 44100 Hz. Both sensors are interfaced with a personal computer running Ubuntu Operating System and an in-house developed software platform utilizing robot operating system (ROS). Audio and visual data were captured simultaneously during the experiments through this software, as detailed in our previous studies [48–50].

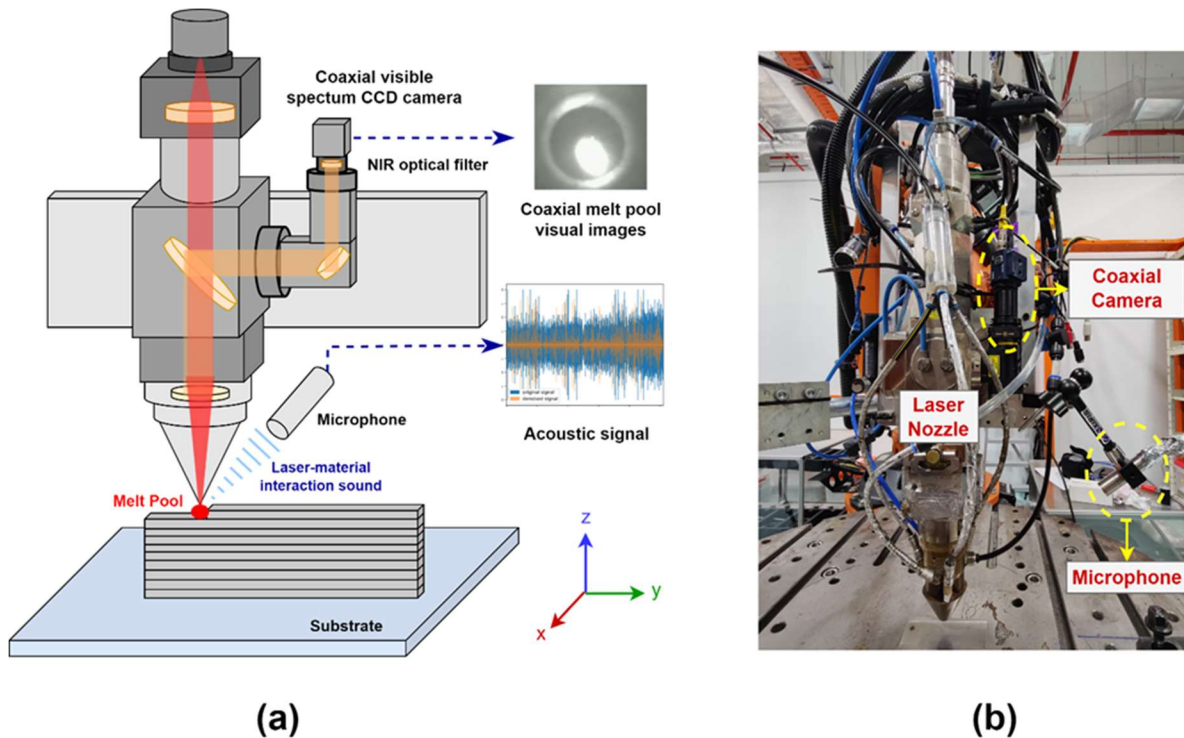


**Figure 2: LDED system with coaxial melt pool camera and acoustic sensor setups: (a) schematic illustration and (b) experiment photo.**



The audio-visual multimodal dataset was created with LDED of single-bead walls with maraging steel C300 powder. Table 1 presents the process parameters employed during the experiments. In this study, we opted not to introduce defects deliberately by using suboptimal parameters. Instead, parameters were pre-optimized to achieve near fully-dense quality, suitable for multi-layer, multi-track industrial production. However, due to limited heat transfer capacities, localized heat accumulation was exacerbated during the fabrication of single-bead wall samples. This led to rapid heating and cooling cycles, resulting in the emergence of defects such as cracks and keyhole pores gradually during the deposition. After several layers of printing, a transition from defect-free to defective zones was observed. Consequently, data points from these regions were categorized as “defective”. The dataset thus comprises three annotated categories: defective, non-defective, and laser-off. The example dataset has been open-sourced and is available for download for interested readers [74].

**Table 1: LDED process parameters and setup information for audio-visual data collection experiments.**

Parameters	Values
Part geometry	Single bead wall structure
Laser power (kW)	2.3-2.5
Speed (mm/s)	25-27.5
Dwell time between the layers (s)	[0, 5, 10]
Laser beam diameter (mm)	2
Powder flow rate (g/min)	12
Energy density (kW·s /mm)	0.92
Hatch space (mm)	1
Layer thickness (mm)	0.85
Stand-off distance (mm)	12
Material	Maraging Steel C300
Types of defects generated	Cracks, keyhole pores

Data handling techniques were applied to prepare and preprocess the multimodal data for subsequent knowledge transfer and prediction tasks. First, data synchronization and registration were conducted as illustrated in [49]. The audio data was segregated into audio snippets of 33.3 milliseconds according to the acquisition frequency of the visual data (Figure 3). Each audio snippet stored the audio signals collected between two adjacent melt pool images. The same label was shared between an audio snippet and the melt pool image captured at the beginning of the snippet. Afterward, each melt pool image was resized from  $480 \times 480$  pixels to  $80 \times 80$  pixels to reduce the dimensionality while retaining most of the information. Each audio snippet was converted to a spectrogram, which is proven efficient for extracting salient audio features [75]. The horizontal axis, vertical axis, and color scale of a spectrogram represent the time, frequency, and magnitude of the audio, respectively. The parameters were adjusted to output spectrograms of  $80 \times 80$  pixels to align with the visual data. The spectrograms were converted to grayscale images for dimensionality reduction. The experiment yielded 4345 melt pool images and audio snippets, which were split into a training set, a validation set, and a test set at a ratio of 8:1:1. The data size of each sub-dataset is presented in Table 2.

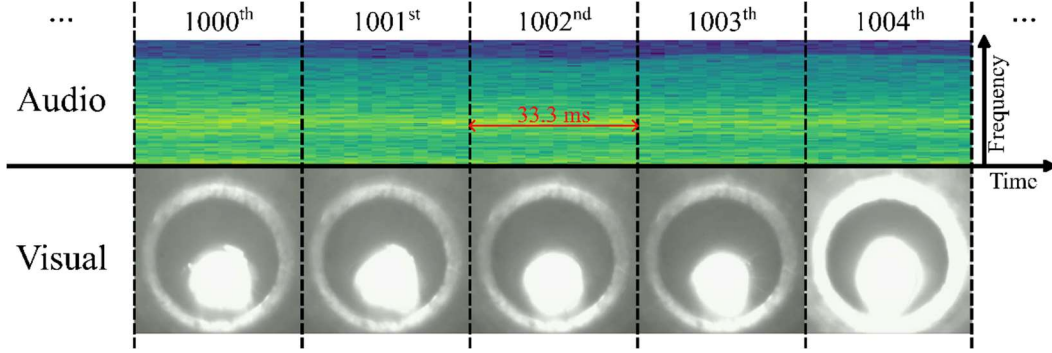


Figure 3: Synchronized and registered audio data (converted to spectrograms) and visual data (melt pool images).

Table 2: Train-validation-test split of the dataset.

Datasets	Defect-free	Defective
Training	859	2617
Validation	112	322
Test	114	321

### 3.2. Cross-modality knowledge transfer

Knowledge transfer, including transfer learning and domain adaptation, involves knowledge sharing between a source and a target [76]. In transfer learning, the tasks (i.e., output variables) of the source and target are different, while the input domain remains the same. CMKT belongs to domain adaptation, where the input domains are different between the source and target, while the task remains the same ( $\mathcal{Y}_V = \mathcal{Y}_A$ ). The multimodal AM in-situ monitoring system illustrated in Figure 2 involves a visual dataset ( $D_V$ ) and an audio dataset ( $D_A$ ). The visual dataset ( $D_V = \{(x_{V,1}, y_{V,1}), \dots, (x_{V,n_V}, y_{V,n_V})\}$ ) with a data size of  $n_V$  is collected using the coaxial camera, where  $x_{V,i} \in X_V$  and  $y_{V,i} \in Y_V$  are the  $i^{\text{th}}$  melt pool image and the corresponding label, respectively. The audio dataset ( $D_A = \{(x_{A,1}, y_{A,1}), \dots, (x_{A,n_A}, y_{A,n_A})\}$ ) with a data size of  $n_A$  is collected using the microphone, where  $x_{A,i} \in X_A$  and  $y_{A,i} \in Y_A$  are the  $i^{\text{th}}$  spectrogram and the corresponding label, respectively. The input domains in this setting have different feature spaces ( $X_V \neq X_A$ ) and marginal probability distributions ( $P(X_V) \neq P(X_A)$ ). In CMKT, both  $D_V$  and  $D_A$  can be used to train the model, while only the input of one modality ( $X_V$  or  $X_A$ ) is need for making predictions. Knowledge can be transferred from the visual modality to the audio modality, or from the audio modality to the visual modality. The remaining modality at the prediction phase is the target modality (Figure 1b). This paper proposes three CMKT methods for AM in-situ monitoring: semantic alignment, fully supervised mapping, and semi-supervised mapping

### 3.2.1. Semantic alignment

The first proposed method utilizes classification and contrastive semantic alignment (CCSA) [77]. Semantic alignment conducts knowledge transfer by aligning the source and the target distributions in an encoded space [77]. The CCSA architecture adapted for CMKT is presented in Figure 4, which illustrates the model structure, loss terms, and forward and backward propagations. The model structure consists of a convolutional encoder ( $G_e$ ) and a task classifier ( $G_t$ ), which are both shared between the visual and audio modalities.  $G_e$  extracts salient representations from visual and audio input data utilizing concatenated convolution layers, pooling layers, and activation functions. An encoded space, constructed by  $G_e$ , semantically aligns the visual and audio distributions using a contrastive semantic alignment loss ( $L_{CSA}$ ):

$$L_{CSA} = L_{SA} + L_S, \quad (1)$$

where  $L_{SA}$  and  $L_S$  are semantic alignment loss and separation loss, respectively.  $L_{SA}$  encourages  $G_e$  to aggregate samples with the same labels from different modalities in the encoded space:

$$L_{SA}(G_e) = \sum_{a=1}^C d\left(p(G_e(X_V^a)), p(G_e(X_A^a))\right), \quad (2)$$

where  $C$  is the number of classes,  $d$  is a distance metric between two distributions,  $X_V^a = X_V|Y=a$  and  $X_A^a = X_A|Y=a$ .  $L_S$  penalizes the similarity between samples with different labels from different modalities in the encoded space:

$$L_S(G_e) = \sum_{a,b|a \neq b} k\left(p(G_e(X_V^a)), p(G_e(X_A^b))\right), \quad (3)$$

where  $k$  is a similarity metric. To learn a shared encoded space for both modalities,  $G_e$  utilizes a Siamese network shared between the visual and audio data [78]. A shared network also reduces computational complexity. Based on the salient representations extracted by  $G_e$ , a shared task classifier ( $G_t$ ) classifies whether the sample belongs to the defective or defect-free class. At each training epoch,  $G_t$  is updated using the mean classification loss ( $L_C$ ), which is the mean of the visual and audio classification losses ( $L_V$  and  $L_A$ ):

$$L_C(G_e \circ G_t) = [L_V(G_e \circ G_t) + L_A(G_e \circ G_t)]/2. \quad (4)$$

In this paper,  $L_V$  and  $L_A$  are calculated using binary cross entropy. Following the update of  $G_t$ ,  $G_e$  is updated using the CCSA loss:

$$L_{CCSA}(G_e \circ G_t) = (1 - \gamma)(L_{SA}(G_e) + L_S(G_e)) + \gamma L_C(G_e \circ G_t), \quad (5)$$

where  $\gamma$  is a trade-off factor between  $L_C$  and  $L_{CSA}$ . In this way, the two distributions must be well aligned in the encoded space to obtain accurate classifications because  $G_t$  is also shared between the two modalities. In other words, the representations of the two modalities must be similar for securing accurate classifications using the same task classifier.

In a real-life setting, manufacturing datasets almost always face data scarcity. However, both  $L_{SA}$  and  $L_S$  calculates the distributions of the encoded visual and audio data, which demands a large data size. Motiian et al. [77] suggests approximating the distance metric ( $d$ ) by computing the average pairwise distances between the encoded samples:

$$d\left(p(G_e(X_V^a)), p(G_e(X_A^a))\right) = \sum_{i,j} d\left(G_e(x_V^i), G_e(x_A^j)\right), \quad (6)$$

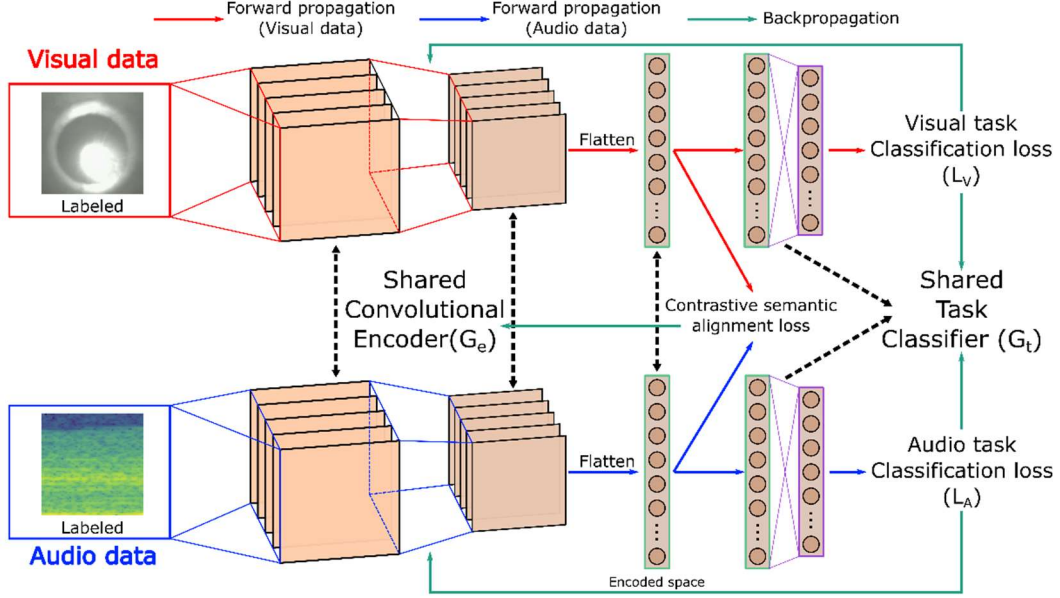


**Figure 4: Schematics of the proposed cross-modal knowledge transfer based on contrastive and classification semantic alignment.**

where  $y_i^V = y_i^A = a$ . Likewise, the similarity metric ( $k$ ) can also be approximated by pairwise distances:

$$k\left(p\left(G_e\left(X_V^a\right)\right), p\left(G_e\left(X_A^b\right)\right)\right)=\sum_{i, j} k\left(G_e\left(x_V^i\right), G_e\left(x_A^j\right)\right), \quad (7)$$

where  $y_V^i = a \neq y_A^j = b$ . It can be further assumed that:

$$d\left(G_e\left(x_V^i\right), G_e\left(x_A^j\right)\right)=\left\|G_e\left(x_V^i\right)-G_e\left(x_A^j\right)\right\|^2 / 2, \quad (8)$$

$$k\left(G_e\left(x_V^i\right), G_e\left(x_A^j\right)\right)=\max \left(0, m-\left\|G_e\left(x_V^i\right)-G_e\left(x_A^j\right)\right\|\right)^2 / 2, \quad (9)$$

where  $\|\cdot\|$  denotes the Euclidean norm and  $m$  is the margin that defines the separability in the encoded space. If knowledge is transferable between the two modalities, a trained modal should be able to extract salient representations and make accurate classifications for both modalities. The model only needs the input data collected from visual or audio sensors to make predictions.

### 3.2.2. Cross-modality mapping

The second proposed strategy conducts knowledge transfer by learning a mapping between two modalities to derive the salient representations of one modality from the other modality (Figure 5). Unlike semantic alignment, mapping requires defining a source and a target. The source modality could be removed during the prediction phase if its salient features are derivable from the target modality. This strategy usually involves multiple phases: Phase 1 utilizes feature learning to extract salient representations, Phase 2 learns a mapping between two modalities, and Phase 3 finetunes the mapping to adapt to the prediction task. The mapping strategy can be categorized into fully supervised (Figure 5a) and semi-supervised (Figure 5b) mappings that extract salient representations using supervised and unsupervised learning, respectively.

### ***Fully supervised mapping***

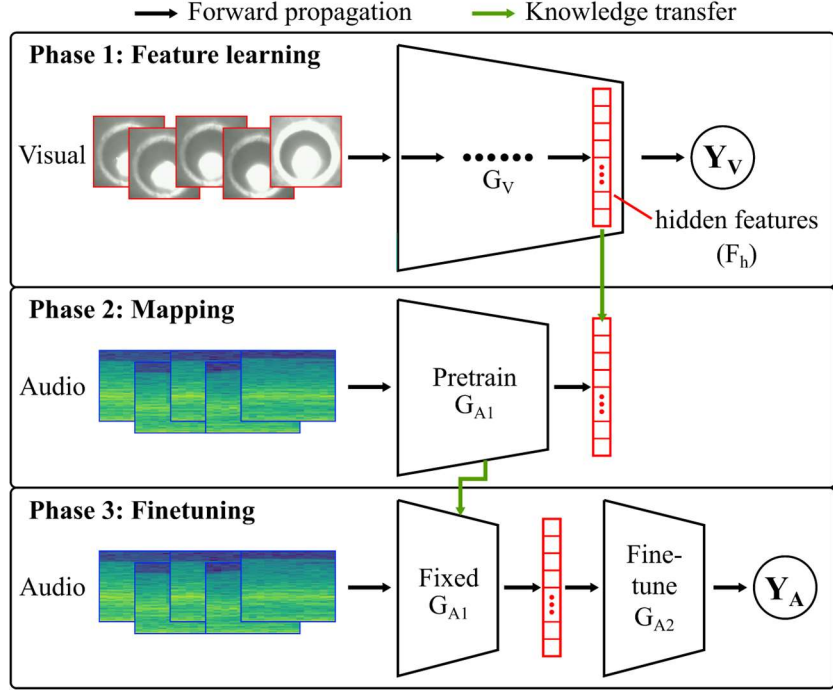
Figure 5a illustrates how fully supervised mapping CMKT can be conducted from the visual domain to the audio domain in three phases. The first phase trains a classification model ( $G_V$ ) purely based on the visual dataset. The classification loss used to train  $G_V$  can be expressed as  $L_V(G_V(X_V), Y_V)$ . The hidden features ( $F_h$ ) that are representative of the classification task are extracted from the last hidden layer of  $G_V$ . The second phase utilizes  $F_h$  to train a mapping,  $G_{A1}$ , and guide the feature extraction from audio samples, which conducts knowledge transfer from the visual modality to the audio modality.  $G_{A1}$  is trained to minimize  $L_{A1}(G_{A1}(X_A), F_h)$ . In the third phase,  $G_{A1}$  is fixed to extract  $F_h$  from audio samples, followed by additional hidden layers ( $G_{A2}$ ) to make a classification based on  $F_h$ . The classification loss used to train  $G_{A2}$  can be expressed as  $L_{A2}(G_{A2}(F_h), Y_A)$ . This method can also transfer knowledge from the audio to the visual modality by switching the positions of the two modalities in Figure 5a. In this way,  $G_{A1}$  learns to derive the hidden feature of the audio modality from the visual modality. However, the features extracted from the visual modality are usually more effective for melt pool anomaly detection than the features from the audio modality. Thus, knowledge transfer from the audio to the visual modality might lead to compromised classification performance.

### ***Semi-supervised mapping***

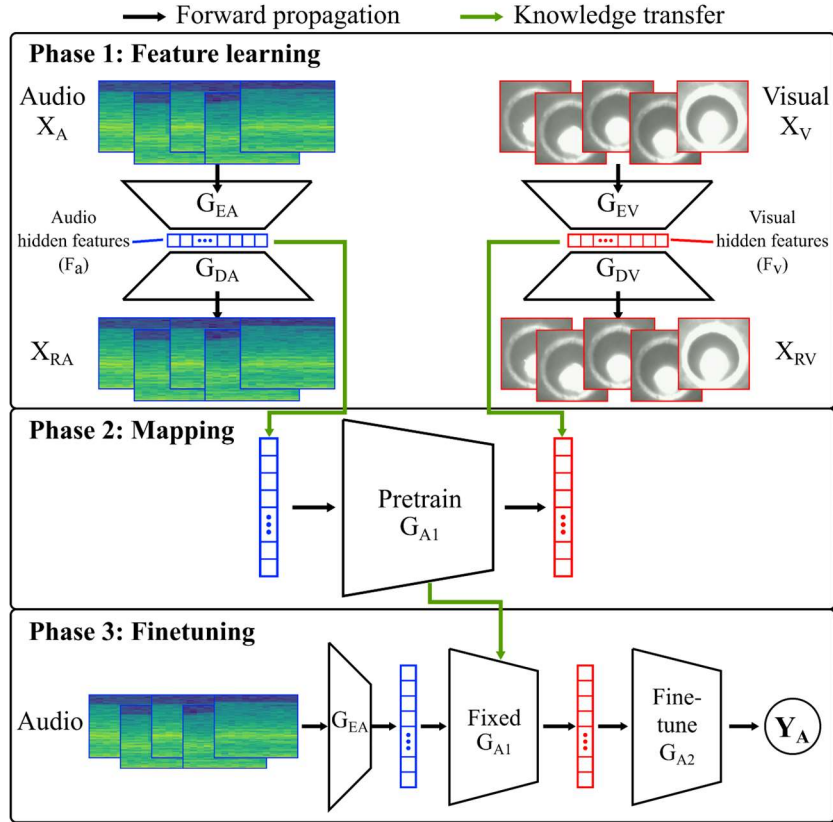
Figure 5b illustrates how semi-supervised mapping CMKT can be conducted from the visual domain to the audio domain in three phases. The first phase separately trains two autoencoders:  $G_V$  consisting of  $G_{EV}$  and  $G_{DV}$  based on  $X_V$  and  $G_A$  consisting of  $G_{EA}$  and  $G_{DA}$  based on  $X_A$ . The reconstruction loss used to train  $G_A$  and  $G_V$  can be expressed as  $L_A(X_A, X_{RA})$  and  $L_V(X_V, X_{RV})$  respectively where subscript ‘R’ represents reconstructed inputs. The hidden features ( $F_a$  and  $F_v$ ) that are representative of the input modalities are extracted from the bottleneck layers of  $G_A$  and  $G_V$ , respectively. The second phase utilizes  $F_a$  and  $F_v$  to train a model,  $G_{A1}$ , and guide the feature mapping from audio to visual hidden features, which conducts knowledge transfer from the visual modality to the audio modality.  $G_{A1}$  is trained to minimize  $L_{A1}(F_a, F_v)$ . In the third phase,  $G_A$  and  $G_{A1}$  are fixed to extract  $F_v$  from audio samples, followed by an additional model ( $G_{A2}$ ) to make a classification based on  $F_v$ . The classification loss used to train  $G_{A2}$  can be expressed as  $L_{A2}(G_{A2}(G_{A1}(G_{EA}(X_A))), Y_A)$ . By switching the direction of the forward propagation at Phase 2 of Figure 5b, this method can also transfer knowledge from the audio modality to the visual modality. In this setting,  $G_{A1}$  learns to map the features from the visual modality to the audio modality. However, as highlighted by the related research, the features extracted from the visual modality are usually more information-rich and thus effective for the melt pool anomaly detection than the features from the audio modality.

## **4. Results**

This section demonstrates the training and evaluation of the proposed CMKT methods. As a comparison, three multimodal fusion methods, including data-level fusion, feature-level fusion, and decision-level fusion, were implemented and evaluated in this section. Besides, single-modal methods (i.e., visual-data-only and audio-data-only) were implemented as the baselines. Hyperparameter searches were conducted to select the optimal models and investigate the performance of each method. Finally, the methods were evaluated using three metrics namely accuracy, area under the receiver operating characteristics curve (AUC-ROC), and balanced accuracy.



(a)



(b)

Figure 5: Schematics of the cross-modality mapping methods: (a) fully supervised mapping and (b) semi-supervised mapping.

#### 4.1. Model training and hyperparameter search

Comprehensive hyperparameter searches were performed to establish a fair comparison and to obtain the optimal performance of the CMKT and multimodal fusion methods. For each method, 300 candidate models were trained using the training set and evaluated using the validation set. For example, Table 3 presents the model settings and hyperparameter ranges of an extensive hyperparameter search conducted for the semantic alignment CMKT method. This hyperparameter search explored a wide range of learning rates, numbers of convolution layers, numbers of filters, kernel sizes, numbers of fully connected layers, numbers of neurons, and dropout rates. According to the literature and preceding training results, a separability margin ( $m$ ) of 1, a trade-off factor ( $\gamma$ ) of 0.5, and 1200 training epochs were selected to ensure convergence. The training process also deployed class weighting to address class imbalance in the dataset. The hyperparameter search employed Bayesian optimization that maximized the validation accuracy to obtain the optimal hyperparameters. We conducted the hyperparameter search using Optuna [79].

**Table 3: Model settings and hyperparameter search of the semantic alignment CMKT method.**

Fixed hyperparameter/setting	Value/method
Activation	ReLU
Optimizer	Adam
$L_V$ and $L_A$	Binary cross entropy
Class weighting	defective/defect-free=1/3
$L_{CCSA}$	$(1 - \gamma)(L_{SA} + L_S) + \gamma(L_V + L_A)/2$
Input and output layer dimensions	$80 \times 80$ and 1
Separability margin ( $m$ )	1
Trade-off factor ( $\gamma$ )	0.5
Learning rate	$(x \in \mathbb{R}   1E^{-6} \leq x \leq 1E^{-3})$
Weight decay	$(x \in \mathbb{R}   1E^{-7} \leq x \leq 1E^{-3})$
Number of epochs	1200
<b>Convolutional encoder (<math>G_e</math>)</b>	
Tuned hyperparameters	Range
Number of convolution layers	$(x \in \mathbb{N}   3 \leq x \leq 5)$
Number of filters at each convolution layer	$(x \in \mathbb{N}   16 \leq x \leq 48)$
Kernel size at each convolution layer	$(x \in \mathbb{N}   2 \leq x \leq 4)$
<b>Task classifier (<math>G_t</math>)</b>	
Tuned hyperparameters	Range
Number of fully connected layers	$(x \in \mathbb{N}   1 \leq x \leq 3)$
Number of neurons at each hidden layer	$(x \in \mathbb{N}   32 \leq x \leq 360)$
Dropout rate	$(x \in \mathbb{R}   0.01 \leq x \leq 0.1)$

The top 50 models with the highest validation accuracies were selected and trained again to evaluate their test performance and reproducibility. The structure of the optimal model that achieved the highest validation accuracy was recorded in Table 4. It was a deep CNN model consisting of 5 convolutional modules in  $G_e$  and 3 linear modules in  $G_t$ . The model incorporated regularization techniques including weight decay and dropout to mitigate overfitting during training. The loss and accuracy curves can be found in Figure 6. Both  $L_{CCSA}$  and  $L_C$  rapidly

descended in the first 400 epochs, then slowly converged at the 1200<sup>th</sup> epoch. As a combination of  $L_{CSA}$  and  $L_C$ ,  $L_{CCSA}$  followed the same trend as the two loss terms. A decreasing  $L_{CSA}$  indicated that the source and target distributions were being mixed and that the examples of the same class were being aligned in the encoded space. A decreasing  $L_C$  implied that  $G_t$  was learning to classify defect and defect-free examples in both the source and target modalities. Consequently, the training accuracy also increased at the same pace as  $L_C$ .

**Table 4: The optimal hyperparameters of the semantic alignment CMKT model.**

Common settings	
Initial learning rate	0.0007322092
Weight decay	0.0005568733
Convolutional encoder ( $G_e$ )	
Layer	Hyperparameters
1 <sup>st</sup> Convolutional module	Conv2d (31channels, kernel size=2, stride=1, padding= ‘same’), ReLU(), MaxPool2d (kernel size=2, stride=1)
2 <sup>nd</sup> Convolutional module	Conv2d (31 channels, kernel size=2, stride=1, padding= ‘same’), ReLU(), MaxPool2d (kernel size=1, stride=1)
3 <sup>rd</sup> Convolutional module	Conv2d (31 channels, kernel size=2, stride=1, padding= ‘same’), ReLU(), MaxPool2d (kernel size=1, stride=1)
4 <sup>th</sup> Convolutional module	Conv2d (32 channels, kernel size=2, stride=1, padding= ‘same’), ReLU(), MaxPool2d (kernel size=2, stride=1)
5 <sup>th</sup> Convolutional module	Conv2d (32 channels, kernel size=2, stride=1, padding= ‘same’), ReLU(), MaxPool2d (kernel size=2, stride=1)
Flatten	Flatten ( $32 \times 10 \times 10$ )
Task classifiers ( $G_t$ )	
Layer	Hyperparameter/setting
1 <sup>st</sup> Fully connected module	Linear ( $32 \times 10 \times 10$ , 198), ReLU(), Dropout (0.01821)
2 <sup>nd</sup> Fully connected module	Linear (198, 41), ReLU(), Dropout (0.01821)
3 <sup>rd</sup> Fully connected module	Linear (41, 1), sigmoid()

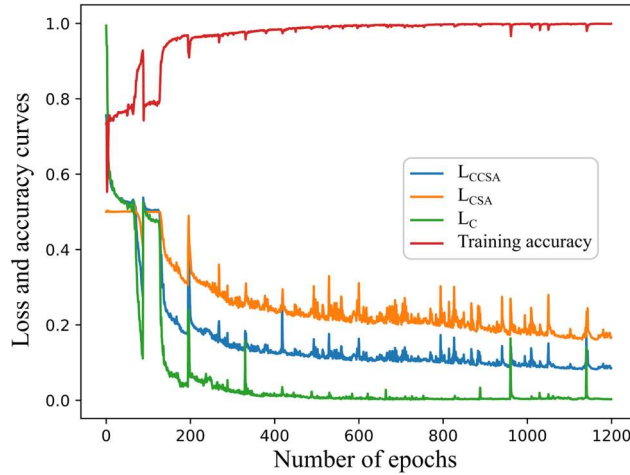


**Figure 6: Loss and training accuracy curves of the semantic alignment CMKT model with the highest validation accuracy.**



The model training and hyperparameter searches of the other implemented methods followed the same procedures as illustrated above. The structures of the optimal fully supervised mapping and semi-supervised mapping models are shown in the appendix (Table A.1 and Table A.2).

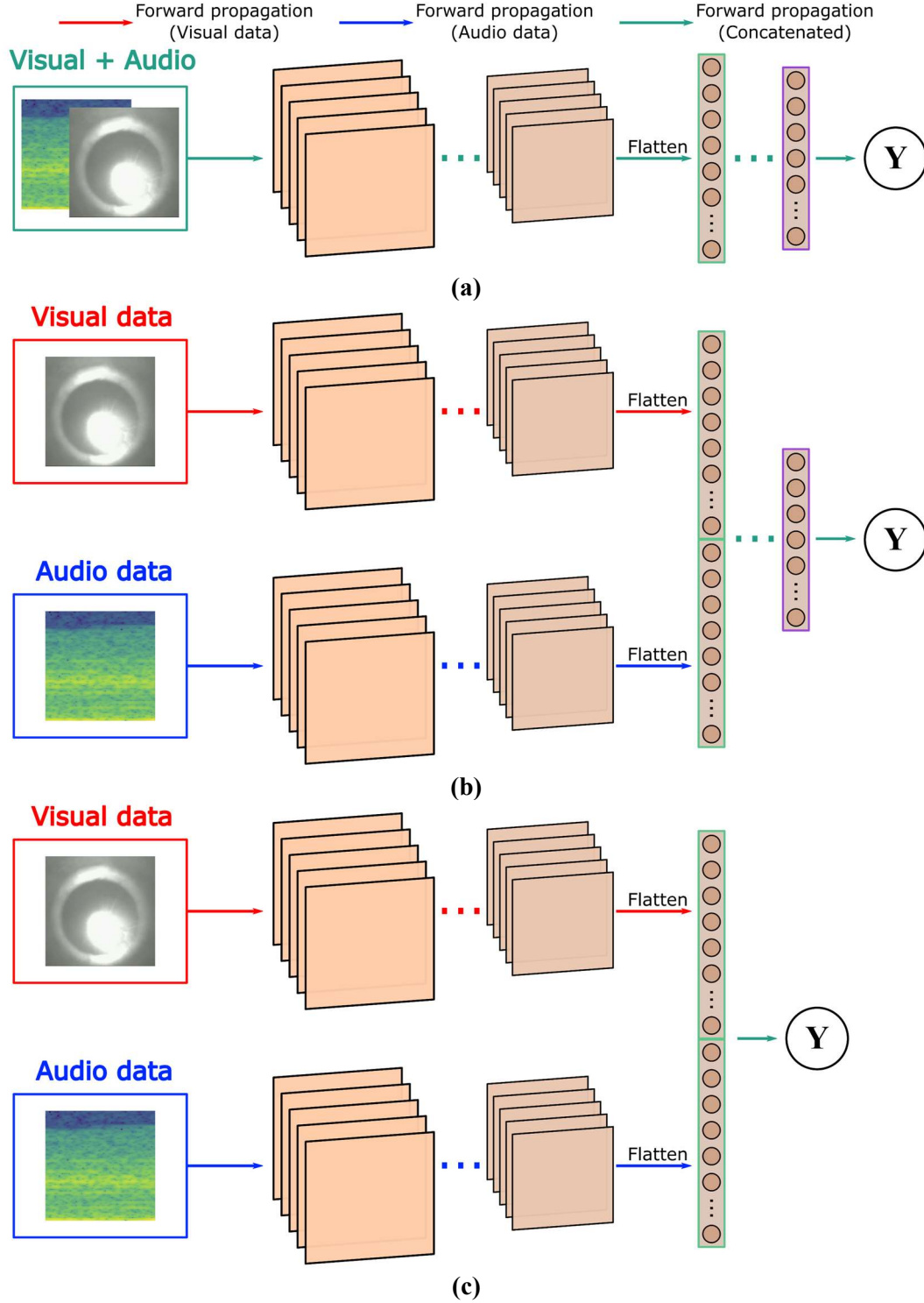


Figure 7: Multimodal fusion (a) data-level fusion; (b) feature-level fusion; and (c) decision-level fusion.

## 4.2. Multimodal fusion

Multimodal fusion methods were also implemented to compare with the proposed CMKT methods. Multimodal fusion is the process that integrates data from several modalities and derives multimodal representations, which are information-rich for the modeling task. Figure 7 exhibits the typical forms of data-level fusion, feature-level fusion, and decision-level fusion. Data-level fusion concatenates the input data of the two modalities, from which multimodal representations are extracted using a single model (Figure 7a). Feature-level fusion separately learns salient representations of each modality, which are then concatenated and fed into subsequent hidden layers. The hidden layers are trained to extract multimodal representations and make predictions (Figure 7b). Decision-level fusion also concatenates the representations learned separately from each modality. However, predictions are directly made based on the concatenated representations with no additional hidden layers (Figure 7c).

## 4.3. Model evaluation

The top models selected from the hyperparameter search of each method were evaluated using the test set based on three metrics: accuracy, AUC-ROC, and balanced accuracy. These three metrics were calculated based on the classification results, including the true positive (TP), true negative (TN), false positive (FP), and false negative (FN). Accuracy is the ratio between the correct predictions and total predictions, which can be obtained using:

$$Accuracy = (TP + TN) / (TP + TN + FP + FN), \quad (10)$$

AUC-ROC evaluates model robustness based on its ability to discriminate between different classes. The ROC curve of a model plots the true positive rate (TPR) against the false positive rate (FPR) at different classification thresholds. Therefore, a large AUC of the ROC curve indicates that the model secures high TPRs and low FPRs across a wide range of thresholds. Balanced accuracy is the arithmetic mean of the TPR and true negative rate (TNR) (*Balanced accuracy* =  $(TPR + TNR) / 2$ ). It accounts for the data imbalance in the dataset because the model performance on both classes is equally weighted.

The test performance of the top 50 models of each method was exhibited in Figures 8 and 9. The bar value, upper limit, and lower limit showed the average, optimal, and minimum scores of the top 50 models, respectively. Models with the highest maximum scores can provide the best performance. Models with high average scores were more robust because most of their selected models could achieve high performance. Models with small ranges (i.e., the difference between the upper and lower limit) can provide consistent performance because most of their selected models achieved similar performance.

As illustrated in Section 3.2.2, the mapping CMKT methods have two knowledge transfer directions: from the visual to audio modality and from the audio to the visual modality. When knowledge is transferred from the audio to the visual modality, the prediction phase takes visual data as input and maps them to the audio modality. Thus, the CMKT of this direction was compared with the visual-data-only single-modal method (Figure 8). When knowledge is transferred from the visual to the audio modality, the prediction phase takes audio data as input and maps them to the visual modality. Thus, the CMKT of this direction was compared with the audio-data-only

single-modal method (Figure 9). Semantic alignment does not map the input to the other modality but to the encoded space shared between the two modalities.

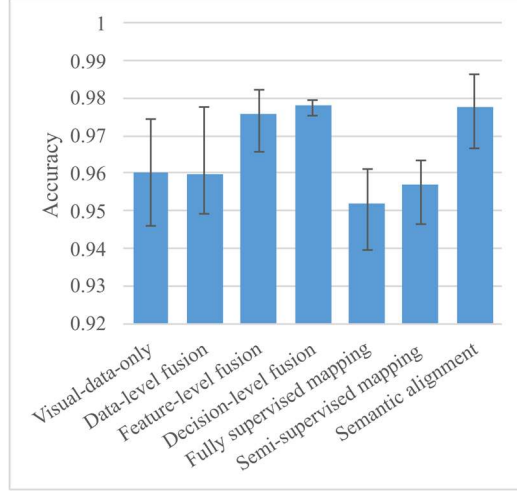
## 5. Discussions

This section provides comprehensive discussions on the performance of the proposed CMKT methods regarding LAM in-situ anomaly detection. It first compares the overall predictive performance of the implemented methods. Then, the advantages of CMKT in ML-based process monitoring were investigated in detail, including higher generalizability, smaller data volume, shorter prediction runtime, and reduced costs. Finally, the limitations of CMKT are discussed.

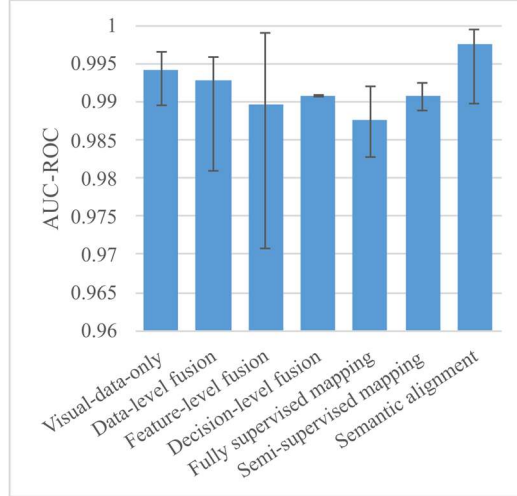
### 5.1. Overall predictive performance

Figure 8 compares the visual-data-only, multimodal fusion, and CMKT methods. The visual-data-only single-modal method achieved an accuracy of 0.974, an AUC-ROC of 0.996, and a balanced accuracy of 0.971. Multimodal fusion provided higher optimal performance than the single-modal method, which aligned with the observations in [15]. The highest optimal accuracy (0.982) and AUC-ROC (0.999) among the multimodal fusion methods were obtained from feature-level fusion. The highest optimal balanced accuracy among the multimodal fusion methods was offered by data-level fusion (0.973). Decision-level fusion provided high average scores and small performance variations, which indicated that it was more consistent and robust. Overall, semantic alignment CMKT achieved the highest optimal accuracy, AUC-ROC, and balanced accuracy, which were 0.984, 0.9995, and 0.981. It also provided the highest or second-highest average and minimum accuracy, AUC-ROC, and balanced accuracy, which indicated its high robustness. Therefore, CMKT can provide comparable and even better predictive performance than multimodal fusion although it involves fewer modalities during the prediction phase. Nonetheless, the two mapping CMKT methods achieved lower scores than the visual-data-only method because they mapped the visual input to the audio modality. The hidden features extracted from the audio modality are usually less effective for LDED process anomaly detection than the visual modality [15].

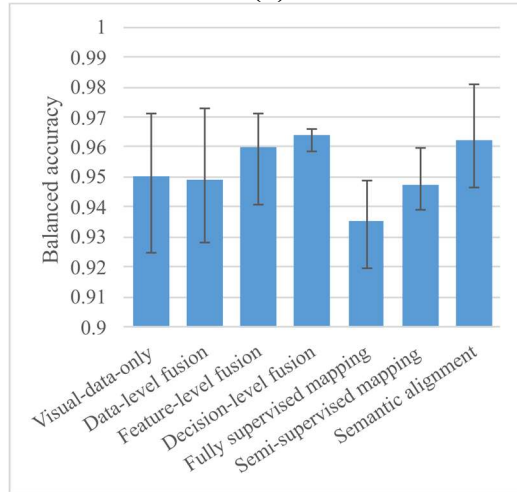
Figure 9 compares the audio-data-only and CMKT methods. This figure does not include multimodal fusion because CMKT cannot achieve comparable predictive performance when taking audio data as input during the prediction phase. The audio-data-only single-modal method achieved an accuracy of 0.946, an AUC-ROC of 0.984, and a balanced accuracy of 0.936. Again, semantic alignment CMKT provided the highest optimal accuracy (0.958), AUC-ROC (0.991), and balanced accuracy (0.960). By mapping the audio data to the visual modality, both fully supervised and semi-supervised mapping CMKT achieved higher optimal and average accuracy and AUC-ROC than the audio-data-only method. However, their optimal balanced accuracies were similar to the audio-data-only method (around 0.94). Therefore, all the proposed CMKT methods can improve the predictive performance while transferring knowledge from the visual to the audio modality. Around 2% increase in accuracy and balanced accuracy was obtained by the semantic alignment CMKT method, which is equivalent to more than 25% error reduction compared to audio-data-only method.



(a)

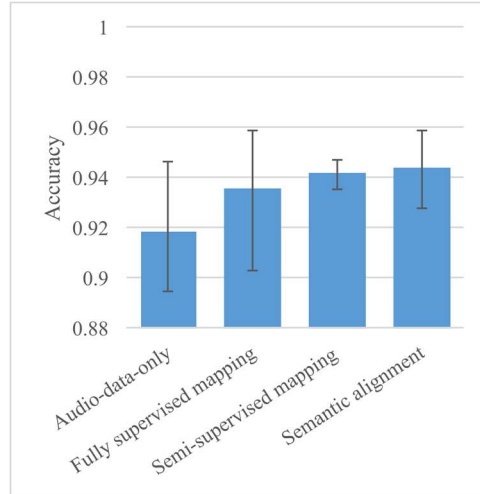


(b)

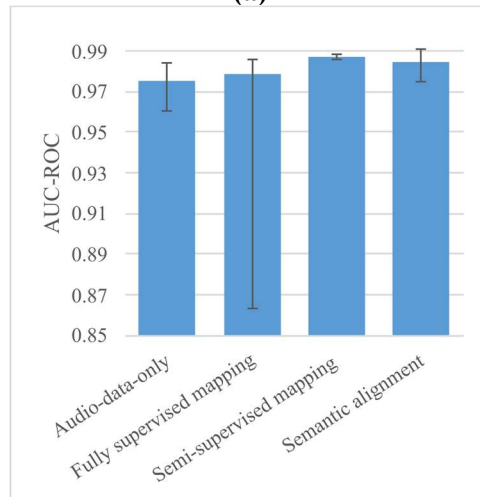


(c)

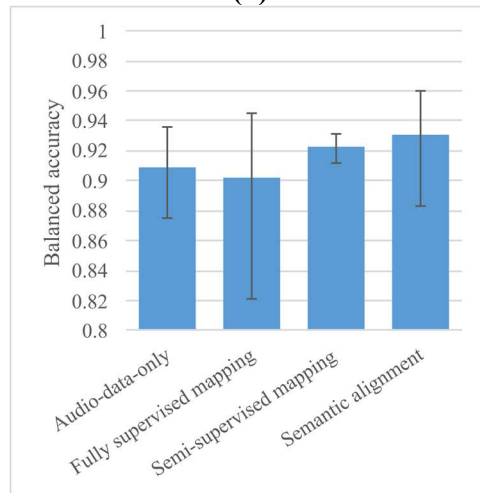
**Figure 8: Performance of the visual-data-only, multimodal fusion, and CMKT methods. (a) accuracy; (b) AUC-ROC; and (c) balanced accuracy. The CMKT models transferred knowledge from the audio to the visual modality.**



(a)



(b)



(c)

**Figure 9: Performance of the audio-data-only and CMKT methods. (a) accuracy; (b) AUC-ROC; and (c) balanced accuracy. The CMKT models transferred knowledge from the visual to the audio modality.**

## 5.2. Computational complexity

Figures 10 and 11 exhibit the training and prediction runtimes of the implemented methods. The training runtimes were the total runtimes accounting for all training epochs, while the prediction runtimes accounted for one forward pass of the validation set through the trained models. The ML models were trained on a Windows 11 system with an Intel Core i7 12<sup>th</sup> Gen processor and an NVIDIA GeForce RTX 4090 GPU, utilizing Python 3.6 and the PyTorch framework. CUDA was employed for GPU acceleration to enhance computational performance during training. The two single-modal methods had the shortest training runtimes with average training runtimes below 70 seconds because they only involved one modality. The average training runtime of data-level fusion (around 400 seconds) was three times higher than feature-level and decision-level fusion. More channels were deployed in the convolutional modules of the data-level fusion models where the two modalities were concatenated at the input layer. The other multimodal fusion methods concatenated the two modalities after the convolutional modules, which reduced the number of weights. The average training runtime of fully supervised mapping (around 80 seconds) was close to feature-level and decision-level fusion (around 100 seconds). The average training runtime of semi-supervised mapping was twice that of fully supervised mapping because semi-supervised mapping trained two autoencoders while fully supervised mapping only trained one CNN in Phase 1. The average training runtime of semantic alignment was the highest among all methods, which was around 750 seconds for both knowledge transfer directions. Semantic alignment had different training and prediction runtimes in Figures 10 and 11 because two batches of the top 50 models were separately chosen using the visual and audio validation sets. Semantic alignment employed semantic alignment loss and separation loss that calculated pairwise distances in the encoded space. Besides, the convolutional encoder and task classifier were updated separately using different loss terms, leading to more computations per epoch and a higher number of epochs to converge.

Although semantic alignment yielded high training runtimes, it had short prediction runtimes (around 0.15 seconds), which were close to the single-modal methods. The semantic alignment model was equivalent to a single-modal CNN model during the prediction phase because no semantic alignment loss or separation loss was computed. The average prediction runtimes of multimodal fusion methods were one to three times higher than semantic alignment because they utilized both modalities when making predictions, while semantic alignment CMKT only involved one modality. The cross-modality mapping methods also had longer prediction runtimes than semantic alignment because they employed multiple networks.

## 5.3. Advantages of cross-modality knowledge transfer

The advantages of the proposed CMKT methods are discussed with respect to the improved model performance and operational efficiency.

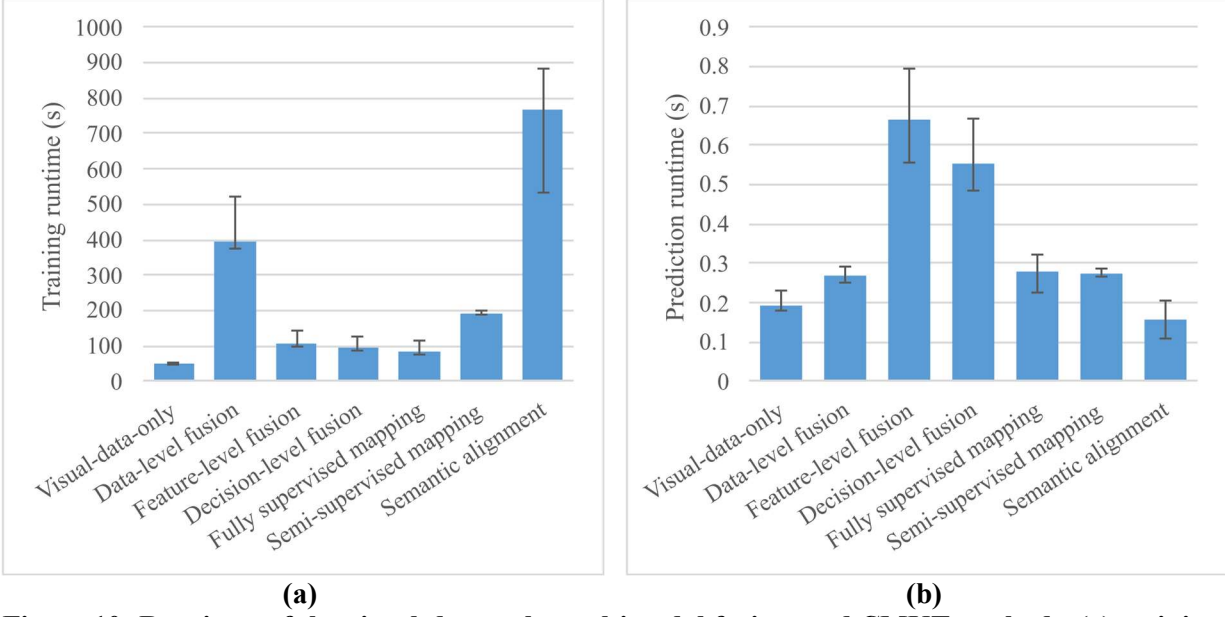


**Figure 10: Runtimes of the visual-data-only, multimodal fusion, and CMKT methods. (a) training runtime and (b) prediction runtime. The CMKT models transferred knowledge from the audio to the visual modality.**

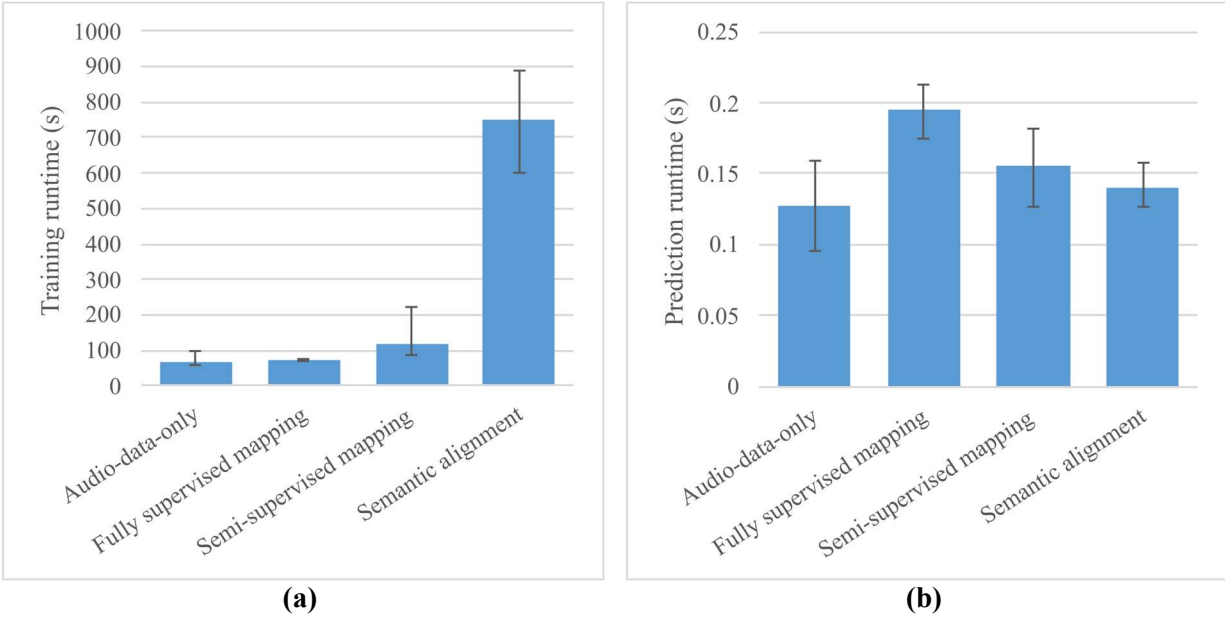


**Figure 11: Runtimes of the audio-data-only and CMKT methods. (a) training runtime and (b) prediction runtime. The CMKT models transferred knowledge from the visual to the audio modality.**

### 5.3.1. Improved model performance

In Figure 12a, the encoded representations of the training data in the optimal semantic alignment model were reduced to two dimensions using t-distributed stochastic neighbor embedding (t-SNE). The cluster contains four groups, including the audio defect-free, audio defective, visual defect-free, and visual defective classes. Compared with the audio modality, the

visual defect-free and defective classes were well split with marginal overlap. This was also reflected in Figures 8 and 9 where the semantic alignment models achieved higher performance when evaluated on visual data than audio data. It was observed that semantic alignment CMKT encouraged the visual defect-free and visual defective classes to split away from each other because of the audio data. The audio data between the visual classes became a buffer zone that increased the distance between the visual defect-free and defective classes, which enhanced the generalizability of the ML model. Figure 12b visualizes the encoded representations of the training data in the last hidden layer of the optimal feature-level fusion model using t-SNE. Compared with semantic alignment CMKT, the fused defect-free and defective classes were close to each other with a long borderline. Therefore, feature-level fusion models were more prone to outliers than semantic alignment CMKT models.

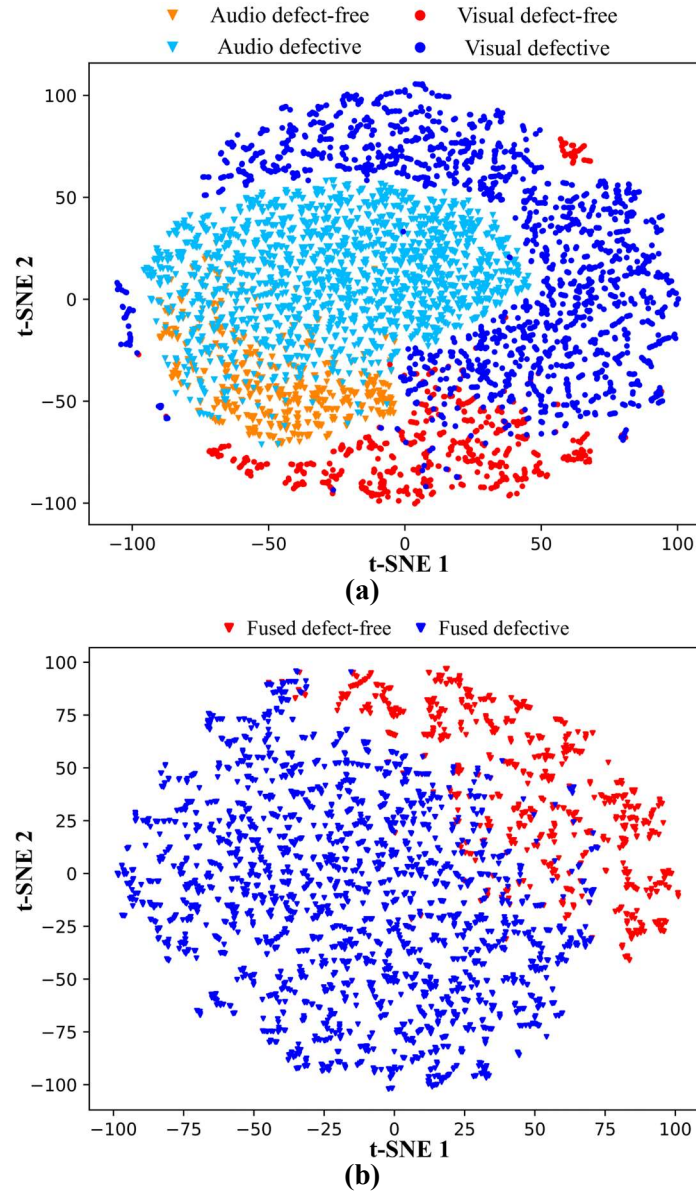


**Figure 12: T-SNE visualization of the encoded space of (a) semantic alignment CMKT and (b) feature-level multimodal fusion.**



The cross-modality mapping CMKT methods offered performance improvement when transferring knowledge from the visual modality to the audio modality. This occurred because the visual features were more effective for LDED in-situ anomaly detection than the audio features. Therefore, the predictive performance was improved when the visual features were derived from the audio modality using cross-modality mapping. However, the performance increase obtained from cross-modality mapping was not as high as semantic alignment.

### **5.3.2. Improved operational efficiency**

CMKT can reduce the data volume and computational complexity of ML-based AM process monitoring systems. After transferring knowledge from the source to the target modality, the source modality can be removed during the prediction phase (i.e., operation). This decreases data volume and execution time for data acquisition, transmission, and preprocessing before making predictions. Thus, the system demands a less powerful computer for local computing and allows faster data transmission to the cloud in an IoT environment. Besides, the architecture of the CMKT models can be more lightweight than multimodal fusion models due to fewer modalities, leading to shorter prediction runtimes (Figures 10 and 11). Additionally, CMKT decreases the number and types of sensors, thus reducing the hardware, operation, and maintenance costs.

### **5.4. Limitations of cross-modality knowledge transfer**

The key underlying assumption of CMKT is that the source and target modalities contain overlapping information about the prediction task. Visual features can be extracted from the visual modality and audio features can be extracted from the audio modality. By transferring knowledge from the source to the target modality, the model can extract more useful features from the target modality than single-modal methods. However, CMKT will not provide performance improvements if the two modalities contain mutually exclusive information (i.e., the features extracted from one modality are not derivable from the other modality) [80]. Further, the training process of CMKT methods is usually more complicated than multimodal fusion methods. Thus, CMKT requires higher training runtimes and ML expertise.

## **6. Conclusions**

This paper proposed CMKT methods that transfer knowledge from the source to the target modality during the training phase, therefore removing the source modality during the prediction phase. In an LDED in-situ anomaly detection case study, the proposed CMKT methods, including semantic alignment, fully supervised mapping, and semi-supervised mapping, were compared with single-modal (i.e., visual-data-only and audio-data-only) and multimodal fusion (i.e., data-level, feature-level, and decision-level fusion) methods. The highest optimal accuracy (98.4%), AUC-ROC (0.9995), and balanced accuracy (98.1%) were obtained using the semantic alignment CMKT method. Although semantic alignment CMKT models took the longest training runtime, their prediction runtimes were much shorter than the multimodal fusion models and close to the single-modal methods. Finally, semantic alignment CMKT offered better generalizability and significantly reduced the computational complexity and costs during the operation. The limitation of CMKT is that the two modalities must contain overlapping information about the prediction task. Otherwise, knowledge may not be transferable between the source and the target modalities.

Future works will focus on the explainability of CMKT to visualize and understand the knowledge transferred across modalities. The proposed CMKT methods will also be extended to other LAM processes such as LPBF and WAAM.

### **Author contributions: CRediT**

**Jiarui Xie:** Conceptualization, Methodology, Software, Validation, Formal analysis, Investigation, Writing - Original Draft, Visualization. **Mutahar Safdar:** Conceptualization, Methodology, Software, Validation, Writing - Original Draft. **Lequn Chen:** Conceptualization, Investigation, Resources, Data Curation, Writing - Original Draft, Supervision, Project administration. **Seung Ki Moon:** Conceptualization, Resources, Writing - Review & Editing, Supervision. **Yaoyao Fiona Zhao:** Conceptualization, Resources, Writing - Review & Editing, Supervision, Funding acquisition.

### **Funding sources**

This work is funded by McGill University Graduate Excellence Fellowship Award [grant number 00157]; Mitacs Accelerate program [grant number IT13369]; McGill Engineering Doctoral Award (MEDA); and National Research Council Canada [NRC INT-015-1]. It is also supported by Agency for Science, Technology and Research (A\*STAR) of Singapore through RIE2025 MTC IAF-PP grant (Grant No. M22K5a0045).

### **Data Availability**

The dataset used in this work is open-source and has been publicly released at Zenodo: <https://zenodo.org/records/12604782>.

## Appendix

**Table A.1: The optimal hyperparameters of the fully supervised mapping method. The models transferred knowledge from the visual to the audio modality.**

Common settings	
Optimizer	Adam
Class weighting	defective/defect-free=1/3
Phase 1: Feature learning ( $G_V$ )	
Initial learning rate	0.0012911986
Loss	Binary cross entropy
Input and output layer dimensions	$80 \times 80$ and 1
Number of epochs	500
<i>Layer</i>	<i>Hyperparameters</i>
1 <sup>st</sup> Convolutional module	Conv2d (30 channels, kernel size=4, stride=1, padding= ‘same’), ReLU(), MaxPool2d (kernel size=2, stride=1)
2 <sup>nd</sup> Convolutional module	Conv2d (30 channels, kernel size=4, stride=1, padding= ‘same’), ReLU(), MaxPool2d (kernel size=1, stride=1)
3 <sup>rd</sup> Convolutional module	Conv2d (30 channels, kernel size=4, stride=1, padding= ‘same’), ReLU(), MaxPool2d (kernel size=2, stride=1)
4 <sup>th</sup> Convolutional module	Conv2d (57 channels, kernel size=4, stride=1, padding= ‘same’), ReLU(), MaxPool2d (kernel size=2, stride=1)
Flatten	Flatten ( $57 \times 10 \times 10$ )
1 <sup>st</sup> Fully connected module	Linear ( $57 \times 10 \times 10$ , 380), ReLU(), Dropout (0.02474)
2 <sup>nd</sup> Fully connected module	Linear (380, 164), ReLU(), Dropout (0.02474)
3 <sup>rd</sup> Fully connected module	Linear (164, 134), ReLU(), Dropout (0.02474), BatchNorm1d
4 <sup>th</sup> Fully connected module	Linear (134, 1), sigmoid
Phase 2: Mapping ( $G_{A1}$ )	
Initial learning rate	0.0026540529
Loss	Mean squared error
Input and output layer dimensions	$80 \times 80$ and 15
Number of epochs	1500
<i>Layer</i>	<i>Hyperparameters</i>
1 <sup>st</sup> Convolutional module	Conv2d (45 channels, kernel size=2, stride=1, padding= ‘same’), ReLU(), MaxPool2d (kernel size=2, stride=1)
2 <sup>nd</sup> Convolutional module	Conv2d (45 channels, kernel size=2, stride=1, padding= ‘same’), ReLU(), MaxPool2d (kernel size=1, stride=1)
3 <sup>rd</sup> Convolutional module	Conv2d (45 channels, kernel size=2, stride=1, padding= ‘same’), ReLU(), MaxPool2d (kernel size=2, stride=1)
4 <sup>th</sup> Convolutional module	Conv2d (54 channels, kernel size=2, stride=1, padding= ‘same’), ReLU(), MaxPool2d (kernel size=2, stride=1)
Flatten	Flatten ( $54 \times 10 \times 10$ )
1 <sup>st</sup> Fully connected module	Linear ( $64 \times 10 \times 10$ , 418), ReLU(), Dropout (0.02955)
2 <sup>nd</sup> Fully connected module	Linear (418, 128), ReLU(), Dropout (0.02955)

3 <sup>rd</sup> Fully connected module	Linear (128, 147), ReLU(), Dropout (0.02955)
4 <sup>th</sup> Fully connected module	Linear (147, 132), ReLU(), Dropout (0.02955)
5 <sup>th</sup> Fully connected module	Linear (132, 78), ReLU(), Dropout (0.02955)
6 <sup>th</sup> Fully connected module	Linear (78, 15)
<b>Phase 3: Finetuning (<math>G_{A2}</math>)</b>	
Initial learning rate	0.0059795128
Loss	Binary cross entropy
Input and output layer dimensions	15 and 1
Number of epochs	150
<i>Layer</i>	<i>Hyperparameters</i>
1 <sup>st</sup> Fully connected module	Linear (15, 144), ReLU(), Dropout (0.04803)
2 <sup>nd</sup> Fully connected module	Linear (144, 108), ReLU(), Dropout (0.04803)
3 <sup>rd</sup> Fully connected module	Linear (108, 97), ReLU(), Dropout (0.04803)
4 <sup>th</sup> Fully connected module	Linear (97, 36), ReLU(), Dropout (0.04803)
5 <sup>th</sup> Fully connected module	Linear (36, 102), ReLU(), Dropout (0.04803)
6 <sup>th</sup> Fully connected module	Linear (102, 1), sigmoid()

**Table A.2: The optimal hyperparameters of the semi-supervised mapping method. The models transferred knowledge from the visual to the audio modality.**

<b>Common settings</b>	
Optimizer	Adam
Class weighting	defective/defect-free=1/3
<b>Phase 1: Feature learning (<math>G_V</math>)</b>	
Initial learning rate	0.00105828121305257
Loss	Mean Squared Error
Input and output dimensions	$80 \times 80$ and $80 \times 80$
Number of epochs	500
<i>Layer</i>	<i>Hyperparameters</i>
Encoder Module: 1 <sup>st</sup> Convolutional layer	Conv2d (21 channels, kernel size=3, stride=2, padding=1), ReLU ()
Encoder Module: 2 <sup>nd</sup> Convolutional layer	Conv2d (128 channels, kernel size=3, stride=2, padding=1), ReLU ()
Encoder Module: 3 <sup>rd</sup> Convolutional layer	Conv2d (100 channels, kernel size=3, stride=2, padding=1), ReLU ()
Flatten	Flatten ( $100 \times 10 \times 10$ )
Encoder Fully Connected Layer	Linear (10000, 42), ReLU()
Decoder Fully Connected Layer	Linear (42, 10000), ReLU()
Unflatten	Unflatten ( $100 \times 10 \times 10$ )
Decoder Module: 1 <sup>st</sup> Deconvolutional layer	ConvTranspose2d (105 channels, kernel size=3, stride=2, padding=1, output padding=1), ReLU()
Decoder Module: 2 <sup>nd</sup> Deconvolutional layer	ConvTranspose2d (56 channels, kernel size=3, stride=2, padding=1, output padding=1),

	ReLU()
Decoder Module: 3rd Deconvolutional layer	ConvTranspose2d (1 channels, kernel size=3, stride=2, padding=1, output padding=1), Sigmoid()
<b>Phase 1: Feature learning (<math>G_A</math>)</b>	
Initial learning rate	0.000926110702226012
Loss	Mean Squared Error
Input and output layer dimensions	$128 \times 12$ and $128 \times 12$
Number of epochs	500
<b>Layer</b>	<b>Hyperparameters</b>
Encoder Module: 1 <sup>st</sup> Convolutional module	Conv2d (27 channels, kernel size=3, stride=2, padding=1), LeakyReLU(0.01), Dropout(0.119353206904521)
Flatten	Flatten ( $27 \times 64 \times 6$ )
1 <sup>st</sup> Fully connected module	Linear (10368, 89), LeakyReLU(0.01)
2 <sup>nd</sup> Fully connected module	Linear (89, 10368), LeakyReLU(0.01)
Unflatten	Unflatten ( $27 \times 64 \times 6$ )
Decoder Module: 1 <sup>st</sup> Deconvolutional module	ConvTranspose2d (1 channels, kernel size=3, stride=2, padding=1, output padding=1), LeakyReLU(0.01)
<b>Phase 2: Mapping (<math>G_{A1}</math>)</b>	
Initial learning rate	0.0000948439065685934
Loss	Mean squared error
Input and output layer dimensions	89 and 42
Number of epochs	100
<b>Layer</b>	<b>Hyperparameters</b>
1 <sup>st</sup> Fully connected module	Linear (89, 67), ReLU(), Dropout (0.09572)
2 <sup>nd</sup> Fully connected module	Linear (67, 587), ReLU(), Dropout (0.09572)
3 <sup>rd</sup> Fully connected module	Linear (587, 42)
<b>Phase 3: Finetuning (<math>G_{A2}</math>)</b>	
Model	Logistic Regression Classifier
Regularization Penalty	L2 norm
Classification Loss	Binary cross entropy
Solver	lbfgs
Input and output dimensions	42 and 1
<b>Hyperparameters</b>	<b>Values</b>
Tolerance for stopping criteria	0.0001
Number of iterations	150
Random state	42

## References

- [1] I. Gibson, D. Rosen, B. Stucker, M. Khorasani, Additive Manufacturing Technologies, Springer, 2021.
- [2] W.E. Frazier, Metal Additive Manufacturing: A Review, *J. Mater. Eng. Perform.* 23 (2014) 1917–1928. <https://doi.org/10.1007/s11665-014-0958-z>.
- [3] K. Zhu, J.Y.H. Fuh, X. Lin, Metal-Based Additive Manufacturing Condition Monitoring: A Review on Machine Learning Based Approaches, *IEEEASME Trans. Mechatron.* 27 (2022) 2495–2510. <https://doi.org/10.1109/TMECH.2021.3110818>.
- [4] M. Yang, M.K. Keshavarz, M. Vlasea, A. Molavi-Kakhki, Towards full-dense high geometric fidelity parts via binder jetting and controlled sintering, *J. Manuf. Process.* 115 (2024) 180–191. <https://doi.org/10.1016/j.jmapro.2024.02.028>.
- [5] J. Qin, F. Hu, Y. Liu, P. Witherell, C.C.L. Wang, D.W. Rosen, T.W. Simpson, Y. Lu, Q. Tang, Research and application of machine learning for additive manufacturing, *Addit. Manuf.* 52 (2022) 102691. <https://doi.org/10.1016/j.addma.2022.102691>.
- [6] M. Yang, J. Yan, P. Peng, P.D. Enrique, M.K. Keshavarz, M. Vlasea, Surface functionalization of binder jetted steels through super-solidus liquid phase sintering and electro-spark deposition, *Surf. Coat. Technol.* 487 (2024) 130994. <https://doi.org/10.1016/j.surfcoat.2024.130994>.
- [7] S. Mutahar, G. Lamouche, P.P. Paul, G. Wood, Y.F. Zhao, Engineering of Additive Manufacturing Features for Data-Driven Solutions: Sources, Techniques, Pipelines, and Applications., in: *Eng. Addit. Manuf. Featur. Data-Driven Solut.*, Springer, 2023.
- [8] M. Safdar, G. Lamouche, P.P. Paul, G. Wood, Y.F. Zhao, Feature engineering in additive manufacturing, in: *Eng. Addit. Manuf. Featur. Data-Driven Solut.*, Springer, 2023.
- [9] Z. Wang, W. Yang, Q. Liu, Y. Zhao, P. Liu, D. Wu, M. Banu, L. Chen, Data-driven modeling of process, structure and property in additive manufacturing: A review and future directions, *J. Manuf. Process.* 77 (2022) 13–31. <https://doi.org/10.1016/j.jmapro.2022.02.053>.
- [10] L. Chen, G. Bi, X. Yao, J. Su, C. Tan, W. Feng, M. Benakis, Y. Chew, S.K. Moon, In-situ process monitoring and adaptive quality enhancement in laser additive manufacturing: A critical review, *J. Manuf. Syst.* 74 (2024) 527–574. <https://doi.org/10.1016/j.jmsy.2024.04.013>.
- [11] M. Safdar, J. Xie, H. Ko, Y. Lu, G. Lamouche, Y.F. Zhao, Transferability Analysis of Data-Driven Additive Manufacturing Knowledge: A Case Study Between Powder Bed Fusion and Directed Energy Deposition, in: *Vol. 2 43rd Comput. Inf. Eng. Conf. CIE*, American Society of Mechanical Engineers, Boston, Massachusetts, USA, 2023: p. V002T02A078. <https://doi.org/10.1115/DETC2023-116458>.
- [12] S. Fathizadan, F. Ju, Y. Lu, Z. Yang, Deep Spatio-Temporal Anomaly Detection in Laser Powder Bed Fusion, *IEEE Trans. Autom. Sci. Eng.* (2024) 1–13. <https://doi.org/10.1109/TASE.2023.3309927>.
- [13] M. Safdar, Y.F. Li, R. El Haddad, M. Zimmermann, G. Wood, G. Lamouche, P. Wanjara, Y.F. Zhao, Accelerated semantic segmentation of additively manufactured metal matrix composites: Generating datasets, evaluating convolutional and transformer models, and developing the MicroSegQ+ Tool, *Expert Syst. Appl.* 251 (2024) 123974. <https://doi.org/10.1016/j.eswa.2024.123974>.
- [14] Y. Zhang, M. Safdar, J. Xie, J. Li, M. Sage, Y.F. Zhao, A systematic review on data of additive manufacturing for machine learning applications: the data quality, type,

- preprocessing, and management, *J. Intell. Manuf.* 34 (2023) 3305–3340.  
<https://doi.org/10.1007/s10845-022-02017-9>.
- [15] L. Chen, G. Bi, X. Yao, C. Tan, J. Su, N.P.H. Ng, Y. Chew, K. Liu, S.K. Moon, Multisensor fusion-based digital twin for localized quality prediction in robotic laser-directed energy deposition, *Robot. Comput.-Integr. Manuf.* 84 (2023) 102581.  
<https://doi.org/10.1016/j.rcim.2023.102581>.
  - [16] J. Li, X. Zhang, Q. Zhou, F.T.S. Chan, Z. Hu, A feature-level multi-sensor fusion approach for in-situ quality monitoring of selective laser melting, *J. Manuf. Process.* 84 (2022) 913–926. <https://doi.org/10.1016/j.jmapro.2022.10.050>.
  - [17] J. Petrich, Z. Snow, D. Corbin, E.W. Reutzel, Multi-modal sensor fusion with machine learning for data-driven process monitoring for additive manufacturing, *Addit. Manuf.* 48 (2021) 102364. <https://doi.org/10.1016/j.addma.2021.102364>.
  - [18] V. Pandiyan, G. Masinelli, N. Claire, T. Le-Quang, M. Hamidi-Nasab, C. De Formanoir, R. Esmailzadeh, S. Goel, F. Marone, R. Logé, S. Van Petegem, K. Wasmer, Deep learning-based monitoring of laser powder bed fusion process on variable time-scales using heterogeneous sensing and operando X-ray radiography guidance, *Addit. Manuf.* 58 (2022) 103007. <https://doi.org/10.1016/j.addma.2022.103007>.
  - [19] Y. Cai, J. Xiong, H. Chen, G. Zhang, A review of in-situ monitoring and process control system in metal-based laser additive manufacturing, *J. Manuf. Syst.* 70 (2023) 309–326. <https://doi.org/10.1016/j.jmsy.2023.07.018>.
  - [20] D.R. Gunasegaram, A.S. Barnard, M.J. Matthews, B.H. Jared, A.M. Andreaco, K. Bartsch, A.B. Murphy, Machine learning-assisted in-situ adaptive strategies for the control of defects and anomalies in metal additive manufacturing, *Addit. Manuf.* 81 (2024) 104013. <https://doi.org/10.1016/j.addma.2024.104013>.
  - [21] T. Herzog, M. Brandt, A. Trinchi, A. Sola, A. Molotnikov, Process monitoring and machine learning for defect detection in laser-based metal additive manufacturing, *J. Intell. Manuf.* (2023). <https://doi.org/10.1007/s10845-023-02119-y>.
  - [22] L. Chen, G. Bi, X. Yao, J. Su, C. Tan, W. Feng, M. Benakis, Y. Chew, S.K. Moon, In-situ process monitoring and adaptive quality enhancement in laser additive manufacturing: A critical review, *J. Manuf. Syst.* 74 (2024) 527–574. <https://doi.org/10.1016/j.jmsy.2024.04.013>.
  - [23] M. Grasso, A.G. Demir, B. Previtali, B.M. Colosimo, In situ monitoring of selective laser melting of zinc powder via infrared imaging of the process plume, *Robot. Comput.-Integr. Manuf.* 49 (2018) 229–239. <https://doi.org/10.1016/j.rcim.2017.07.001>.
  - [24] M.M. Bappy, C. Liu, L. Bian, W. Tian, Morphological Dynamics-Based Anomaly Detection Towards In Situ Layer-Wise Certification for Directed Energy Deposition Processes, *J. Manuf. Sci. Eng.* 144 (2022) 111007. <https://doi.org/10.1115/1.4054805>.
  - [25] Z. Tang, W. Liu, L. Zhu, Z. Liu, Z. Yan, D. Lin, Z. Zhang, H.-C. Zhang, Investigation on coaxial visual characteristics of molten pool in laser-based directed energy deposition of AISI 316L steel, *J. Mater. Process. Technol.* 290 (2021) 116996. <https://doi.org/10.1016/j.jmatprotec.2020.116996>.
  - [26] G. Bi, C.N. Sun, A. Gasser, Study on influential factors for process monitoring and control in laser aided additive manufacturing, *J. Mater. Process. Technol.* 213 (2013) 463–468. <https://doi.org/10.1016/j.jmatprotec.2012.10.006>.

- [27] G. Bi, A. Gasser, K. Wissenbach, A. Drenker, R. Poprawe, Identification and qualification of temperature signal for monitoring and control in laser cladding, *Opt. Lasers Eng.* 44 (2006) 1348–1359. <https://doi.org/10.1016/j.optlaseng.2006.01.009>.
- [28] L. Chen, X. Yao, N.P.H. Ng, S.K. Moon, In-situ Melt Pool Monitoring of Laser Aided Additive Manufacturing using Infrared Thermal Imaging, in: 2022 IEEE Int. Conf. Ind. Eng. Eng. Manag. IEEM, 2022: pp. 1478–1482. <https://doi.org/10.1109/IEEM55944.2022.9989715>.
- [29] Z. Smoqi, A. Gaikwad, B. Bevans, M.H. Kobir, J. Craig, A. Abul-Haj, A. Peralta, P. Rao, Monitoring and prediction of porosity in laser powder bed fusion using physics-informed melt pool signatures and machine learning, *J. Mater. Process. Technol.* 304 (2022) 117550. <https://doi.org/10.1016/j.jmatprotec.2022.117550>.
- [30] L. Chen, X. Yao, Y. Chew, F. Weng, S.K. Moon, G. Bi, Data-Driven Adaptive Control for Laser-Based Additive Manufacturing with Automatic Controller Tuning, *Appl. Sci.* 10 (2020) 7967. <https://doi.org/10.3390/app10227967>.
- [31] M. Khanzadeh, S. Chowdhury, M. Marufuzzaman, M.A. Tschopp, L. Bian, Porosity prediction: Supervised-learning of thermal history for direct laser deposition, *J. Manuf. Syst.* 47 (2018) 69–82. <https://doi.org/10.1016/j.jmsy.2018.04.001>.
- [32] Z. Ren, L. Gao, S.J. Clark, K. Fezzaa, P. Shevchenko, A. Choi, W. Everhart, A.D. Rollett, L. Chen, T. Sun, Machine learning-aided real-time detection of keyhole pore generation in laser powder bed fusion, *Science* 379 (2023) 89–94. <https://doi.org/10.1126/science.add4667>.
- [33] R. Asadi, A. Queguineur, O. Wiikinkoski, H. Mokhtarian, T. Aihkialo, A. Revuelta, I.F. Ituarte, Process monitoring by deep neural networks in directed energy deposition: CNN-based detection, segmentation, and statistical analysis of melt pools, *Robot. Comput.-Integr. Manuf.* 87 (2024) 102710. <https://doi.org/10.1016/j.rcim.2023.102710>.
- [34] C.S. Lough, T. Liu, X. Wang, B. Brown, R.G. Landers, D.A. Bristow, J.A. Drallmeier, E.C. Kinzel, Local prediction of Laser Powder Bed Fusion porosity by short-wave infrared imaging thermal feature porosity probability maps, *J. Mater. Process. Technol.* 302 (2022) 117473. <https://doi.org/10.1016/j.jmatprotec.2021.117473>.
- [35] S.M. Estalaki, C.S. Lough, R.G. Landers, E.C. Kinzel, T. Luo, Predicting defects in laser powder bed fusion using in-situ thermal imaging data and machine learning, *Addit. Manuf.* 58 (2022) 103008. <https://doi.org/10.1016/j.addma.2022.103008>.
- [36] V. Pandiyan, R. Drissi-Daoudi, S. Shevchik, G. Masinelli, R. Logé, K. Wasmer, Analysis of time, frequency and time-frequency domain features from acoustic emissions during Laser Powder-Bed fusion process, *Procedia CIRP* 94 (2020) 392–397. <https://doi.org/10.1016/j.procir.2020.09.152>.
- [37] B. Bevans, A. Ramalho, Z. Smoqi, A. Gaikwad, T.G. Santos, P. Rao, J.P. Oliveira, Monitoring and flaw detection during wire-based directed energy deposition using in-situ acoustic sensing and wavelet graph signal analysis, *Mater. Des.* 225 (2023) 111480. <https://doi.org/10.1016/j.matdes.2022.111480>.
- [38] L. Chen, X. Yao, S.K. Moon, In-situ acoustic monitoring of direct energy deposition process with deep learning-assisted signal denoising, *Mater. Today Proc.* (2022). <https://doi.org/10.1016/j.matpr.2022.09.008>.
- [39] V. Pandiyan, R. Wróbel, C. Leinenbach, S. Shevchik, Optimizing In-situ Monitoring for Laser Powder Bed Fusion Process: Deciphering Acoustic Emission and Sensor Sensitivity



- with Explainable Machine Learning, *J. Mater. Process. Technol.* (2023) 118144. <https://doi.org/10.1016/j.jmatprotec.2023.118144>.
- [40] R. Drissi-Daoudi, V. Pandiyan, R. Logé, S. Shevchik, G. Masinelli, H. Ghasemi-Tabasi, A. Parrilli, K. Wasmer, Differentiation of materials and laser powder bed fusion processing regimes from airborne acoustic emission combined with machine learning, *Virtual Phys. Prototyp.* 0 (2022) 1–24. <https://doi.org/10.1080/17452759.2022.2028380>.
- [41] D.Y. Kononenko, V. Nikonova, M. Seleznev, J. van den Brink, D. Chernyavsky, An in situ crack detection approach in additive manufacturing based on acoustic emission and machine learning, *Addit. Manuf. Lett.* 5 (2023) 100130. <https://doi.org/10.1016/j.addlet.2023.100130>.
- [42] M. Hamidi Nasab, G. Masinelli, C. de Formanoir, L. Schlenger, S. Van Petegem, R. Esmailzadeh, K. Wasmer, A. Ganvir, A. Salminen, F. Aymanns, F. Marone, V. Pandiyan, S. Goel, R.E. Logé, Harmonizing sound and light: X-ray imaging unveils acoustic signatures of stochastic inter-regime instabilities during laser melting, *Nat. Commun.* 14 (2023) 8008. <https://doi.org/10.1038/s41467-023-43371-3>.
- [43] L. Chen, X. Yao, C. Tan, W. He, J. Su, F. Weng, Y. Chew, N.P.H. Ng, S.K. Moon, In-situ crack and keyhole pore detection in laser directed energy deposition through acoustic signal and deep learning, *Addit. Manuf.* 69 (2023) 103547. <https://doi.org/10.1016/j.addma.2023.103547>.
- [44] H.-S. Kim, S.-H. Park, Acoustic Signal Monitoring Using Audible Cracking Sounds for Efficient In-Situ Crack Detection in Laser Directed Energy Deposition of Hard Surfaces, (2024). <https://doi.org/10.2139/ssrn.4693373>.
- [45] J. Petrich, Z. Snow, D. Corbin, E.W. Reutzel, Multi-modal sensor fusion with machine learning for data-driven process monitoring for additive manufacturing, *Addit. Manuf.* 48 (2021) 102364. <https://doi.org/10.1016/j.addma.2021.102364>.
- [46] A. Vandone, S. Baraldo, A. Valente, Multisensor Data Fusion for Additive Manufacturing Process Control, *IEEE Robot. Autom. Lett.* 3 (2018) 3279–3284. <https://doi.org/10.1109/LRA.2018.2851792>.
- [47] Z. Yang, J. Kim, Y. Lu, A. Jones, P. Witherell, H. Yeung, H. Ko, Enhancing Part Quality Management Using a Holistic Data Fusion Framework in Metal Powder Bed Fusion Additive Manufacturing, *J. Comput. Inf. Sci. Eng.* 24 (2024). <https://doi.org/10.1115/1.4064528>.
- [48] L. Chen, X. Yao, K. Liu, C. Tan, S.K. Moon, MULTISENSOR FUSION-BASED DIGITAL TWIN IN ADDITIVE MANUFACTURING FOR IN-SITU QUALITY MONITORING AND DEFECT CORRECTION, *Proc. Des. Soc.* 3 (2023) 2755–2764. <https://doi.org/10.1017/pds.2023.276>.
- [49] L. Chen, G. Bi, X. Yao, C. Tan, J. Su, N.P.H. Ng, Y. Chew, K. Liu, S.K. Moon, Multisensor fusion-based digital twin for localized quality prediction in robotic laser-directed energy deposition, *Robot. Comput.-Integr. Manuf.* 84 (2023) 102581. <https://doi.org/10.1016/j.rcim.2023.102581>.
- [50] L. Chen, X. Yao, W. Feng, Y. Chew, S.K. Moon, Multimodal Sensor Fusion for Real-Time Location-Dependent Defect Detection in Laser-Directed Energy Deposition, in: *ASME 2023 Int. Des. Eng. Tech. Conf. Comput. Inf. Eng. Conf.*, American Society of Mechanical Engineers Digital Collection, 2023. <https://doi.org/10.1115/DETC2023-110284>.

- [51] J. Li, X. Zhang, Q. Zhou, F.T.S. Chan, Z. Hu, A feature-level multi-sensor fusion approach for in-situ quality monitoring of selective laser melting, *J. Manuf. Process.* 84 (2022) 913–926. <https://doi.org/10.1016/j.jmapro.2022.10.050>.
- [52] V. Pandiyan, G. Masinelli, N. Claire, T. Le-Quang, M. Hamidi-Nasab, C. de Formanoir, R. Esmaeilzadeh, S. Goel, F. Marone, R. Logé, S. Van Petegem, K. Wasmer, Deep learning-based monitoring of laser powder bed fusion process on variable time-scales using heterogeneous sensing and operando X-ray radiography guidance, *Addit. Manuf.* 58 (2022) 103007. <https://doi.org/10.1016/j.addma.2022.103007>.
- [53] N.D. Jamnikar, S. Liu, C. Brice, X. Zhang, In situ microstructure property prediction by modeling molten pool-quality relations for wire-feed laser additive manufacturing, *J. Manuf. Process.* 79 (2022) 803–814. <https://doi.org/10.1016/j.jmapro.2022.05.013>.
- [54] B. Bevans, C. Barrett, T. Spears, A. Gaikwad, A. Riensche, Z. Smoqi, H. (Scott) Halliday, P. Rao, Heterogeneous sensor data fusion for multiscale, shape agnostic flaw detection in laser powder bed fusion additive manufacturing, *Virtual Phys. Prototyp.* 18 (2023) e2196266. <https://doi.org/10.1080/17452759.2023.2196266>.
- [55] H. Liu, C. Gobert, K. Ferguson, B. Abranovic, H. Chen, J.L. Beuth, A.D. Rollett, L.B. Kara, Inference of highly time-resolved melt pool visual characteristics and spatially-dependent lack-of-fusion defects in laser powder bed fusion using acoustic and thermal emission data, (2023). <https://doi.org/10.48550/arXiv.2310.05289>.
- [56] L. Chen, Y. Chew, W. Feng, S.K. Moon, Inference of Melt Pool Visual Characteristics in Laser Additive Manufacturing using Acoustic Signal Features and Robotic Motion Data, in: 2024. <https://easychair.org/publications/preprint/4KBp>.
- [57] Y. Tang, M. Rahmani Dehaghani, G.G. Wang, Review of transfer learning in modeling additive manufacturing processes, *Addit. Manuf.* 61 (2023) 103357. <https://doi.org/10.1016/j.addma.2022.103357>.
- [58] F.G. Fischer, M.G. Zimmermann, N. Praetzs, C. Knaak, Monitoring of the powder bed quality in metal additive manufacturing using deep transfer learning, *Mater. Des.* 222 (2022) 111029. <https://doi.org/10.1016/j.matdes.2022.111029>.
- [59] J. Li, Q. Zhou, X. Huang, M. Li, L. Cao, In situ quality inspection with layer-wise visual images based on deep transfer learning during selective laser melting, *J. Intell. Manuf.* (2021) 1–15. <https://doi.org/10.1007/s10845-021-01829-5>.
- [60] X. Zhu, F. Jiang, C. Guo, D. Xu, Z. Wang, G. Jiang, Surface morphology inspection for directed energy deposition using small dataset with transfer learning, *J. Manuf. Process.* 93 (2023) 101–115. <https://doi.org/10.1016/j.jmapro.2023.03.016>.
- [61] V. Pandiyan, R. Drissi-Daoudi, S. Shevchik, G. Masinelli, T. Le-Quang, R. Logé, K. Wasmer, Deep Transfer Learning of Additive Manufacturing Mechanisms Across Materials in Metal-Based Laser Powder Bed Fusion Process, *J. Mater. Process. Technol.* (2022) 117531. <https://doi.org/10.1016/j.jmatprotec.2022.117531>.
- [62] S.-J. Shin, S.-H. Hong, S. Jadhav, D.B. Kim, Detecting balling defects using multisource transfer learning in wire arc additive manufacturing, *J. Comput. Des. Eng.* 10 (2023) 1423–1442. <https://doi.org/10.1093/jcde/qwad067>.
- [63] J. Li, J. Hu, Q. Zhou, Y. Zhang, Transfer learning-based quality monitoring of laser powder bed fusion across materials, *Expert Syst. Appl.* 252 (2024) 124150. <https://doi.org/10.1016/j.eswa.2024.124150>.

- [64] C. Lu, X. Jia, J. Lee, J. Shi, Knowledge transfer using Bayesian learning for predicting the process-property relationship of Inconel alloys obtained by laser powder bed fusion, *Virtual Phys. Prototyp.* 17 (2022) 787–805. <https://doi.org/10.1080/17452759.2022.2068447>.
- [65] V. Pandiyan, R. Wróbel, R.A. Richter, M. Leparoux, C. Leinenbach, S. Shevchik, Monitoring of Laser Powder Bed Fusion process by bridging dissimilar process maps using deep learning-based domain adaptation on acoustic emissions, *Addit. Manuf.* 80 (2024) 103974. <https://doi.org/10.1016/j.addma.2024.103974>.
- [66] M. Safdar, J. Xie, G. Lamouche, H. Ko, Y. Lu, Y.F. Zhao, TRANSFERABILITY ANALYSIS OF DATA-DRIVEN ADDITIVE MANUFACTURING KNOWLEDGE: A CASE STUDY BETWEEN POWDER BED FUSION AND DIRECTED ENERGY DEPOSITION, (n.d.).
- [67] C. Athanasiadis, E. Hortal, S. Asteriadis, Audio–visual domain adaptation using conditional semi-supervised Generative Adversarial Networks, *Neurocomputing* 397 (2020) 331–344. <https://doi.org/10.1016/j.neucom.2019.09.106>.
- [68] S. Zhang, M. Chen, J. Chen, Y.-F. Li, Y. Wu, M. Li, C. Zhu, Combining cross-modal knowledge transfer and semi-supervised learning for speech emotion recognition, *Knowl.-Based Syst.* 229 (2021) 107340. <https://doi.org/10.1016/j.knosys.2021.107340>.
- [69] M. Planamente, C. Plizzari, E. Alberti, B. Caputo, Cross-Domain First Person Audio-Visual Action Recognition through Relative Norm Alignment, (2021). <https://doi.org/10.48550/arXiv.2106.01689>.
- [70] Y. Zhang, H. Doughty, L. Shao, C.G.M. Snoek, Audio-Adaptive Activity Recognition Across Video Domains, in: 2022 IEEE CVF Conf. Comput. Vis. Pattern Recognit. CVPR, IEEE, New Orleans, LA, USA, 2022: pp. 13781–13790. <https://doi.org/10.1109/CVPR52688.2022.01342>.
- [71] C. Cangea, P. Veličković, P. Liò, XFlow: Cross-modal Deep Neural Networks for Audiovisual Classification, *IEEE Trans. Neural Netw. Learn. Syst.* 31 (2020) 3711–3720. <https://doi.org/10.1109/TNNLS.2019.2945992>.
- [72] M. Guo, C. Zhou, J. Liu, Jointly Learning of Visual and Auditory: A New Approach for RS Image and Audio Cross-Modal Retrieval, *IEEE J. Sel. Top. Appl. Earth Obs. Remote Sens.* 12 (2019) 4644–4654. <https://doi.org/10.1109/JSTARS.2019.2949220>.
- [73] L. Chen, X. Yao, P. Xu, S.K. Moon, G. Bi, Rapid surface defect identification for additive manufacturing with in-situ point cloud processing and machine learning, *Virtual Phys. Prototyp.* 16 (2020) 50–67. <https://doi.org/10.1080/17452759.2020.1832695>.
- [74] L. Chen, Acoustic Monitoring Dataset for Robotic Laser Directed Energy Deposition (LDED) of Maraging Steel C300, (2023). <https://doi.org/10.5281/zenodo.10208372>.
- [75] L. Wyse, Audio Spectrogram Representations for Processing with Convolutional Neural Networks, (2017). <https://doi.org/10.48550/ARXIV.1706.09559>.
- [76] J. Wang, C. Lan, C. Liu, Y. Ouyang, T. Qin, W. Lu, Y. Chen, W. Zeng, P.S. Yu, Generalizing to Unseen Domains: A Survey on Domain Generalization, (2021). <https://doi.org/10.48550/ARXIV.2103.03097>.
- [77] S. Motiian, M. Piccirilli, D.A. Adjeroh, G. Doretto, Unified Deep Supervised Domain Adaptation and Generalization, in: 2017 IEEE Int. Conf. Comput. Vis. ICCV, IEEE, Venice, 2017: pp. 5716–5726. <https://doi.org/10.1109/ICCV.2017.609>.
- [78] V.K.B. G, G. Carneiro, I. Reid, Learning Local Image Descriptors with Deep Siamese and Triplet Convolutional Networks by Minimising Global Loss Functions, (2015). <https://doi.org/10.48550/ARXIV.1512.09272>.

- [79] T. Akiba, S. Sano, T. Yanase, T. Ohta, M. Koyama, Optuna: A Next-generation Hyperparameter Optimization Framework, (2019).  
<https://doi.org/10.48550/ARXIV.1907.10902>.
- [80] J. Williams, A. Tadesse, T. Sam, H. Sun, G.D. Montanez, Limits of Transfer Learning, (2020). <https://doi.org/10.48550/ARXIV.2006.12694>.